Johann Wolfgang Goethe-Universität
Frankfurt am Main
Fachbereich Physik
Institut für Theoretische Physik

Master Thesis

Hybrid static potentials in SU(3) gauge theory on the lattice

Christian Reisinger

March 16, 2017

Supervisor
Prof. Dr. Marc Wagner
Institut für Theoretische Physik
Universität Frankfurt a.M.

Second Supervisor
Prof. Dr. Owe Philipsen
Institut für Theoretische Physik
Universität Frankfurt a.M.

Eigenständigkeitserklärung

Hiermit erkäre ich, dass nach §30 Abs. 12 der Studienordnung des Fachbereichs 13 (Physik) der Goethe-Universität Frankfurt am Main vom 24.09.2013 diese Arbeit von mir selbstständig und ausschließlich unter Verwendung der in den Quellen angegebenen Hilfsmittel erarbeitet und verfasst wurde. Zudem erkläre ich, dass diese Arbeit zurvor nicht in dieser oder ähnlicher Form zum absolvieren einer anderen Prüfungs- oder Studienleistung eingereicht wurde.

Abstract

In this work we show a method to construct trial states to obtain hybrid static potentials in SU(3) Yang-Mills theory from lattice computations. Static potentials are computed for the states $\Sigma_g^+, \Sigma_g^-, \Sigma_u^+, \Sigma_u^-, \Pi_u, \Pi_g, \Delta_u, \Delta_g$ using 700 gauge configurations generated with a heatbath algorithm using the Wilson gauge action. Both effective potentials and static potentials are shown for a lattice with a lattice spacing of $a \approx 0.093\,\mathrm{fm}$. Some excited states are also shown. Also, we construct trial states with various different operators and discuss their suitability to construct trial states with large overlaps to the energy eigenstates of the desired hybrid states.

Contents

1 Introduction

The strong interaction is one of the fundamental forces of nature. In theoretical physics, it is described by quantum chromo dynamics (QCD). QCD describes the interaction between quarks, the fundamental constituents of matter which come in 6 different flavors, and gluons, which are the gauge bosons of QCD. QCD is a non-abelian gauge theory of the SU(3)-color gauge group. The non-abelian property of QCD leads to self-interactions of its gauge bosons, which are called gluons. These self-interactions cause the strong interaction to behave very different from the electromagnetic interaction, which is described by an abelian gauge theory. One special property of QCD is its large coupling constant at low energies and large distances, which leads to bound states of quarks and gluons. This large coupling constant makes perturbative calculations impossible. Consequently, a different approach is required at this energy scale, such as statistical simulations on a discretized space-time lattice.

In the quark model, bound states of a quark and an antiquark are called mesons. Mesons can be categorized by the quantum numbers for orbital angular momentum, spin, charge conjugation (which transforms a particle into its antiparticle), and parity (corresponding to the inversion of spacial coordinates), which emerge exclusively from the structure of the quark antiquark pair. However, the gluonic field which is responsible for allowing such bound states can itself be excited. We call exotic matter in the form of a quark antiquark pair with additional excitations in the gluon sector *hybrid mesons*. Hybrid mesons carry different quantum numbers than regular mesons in the quark model, as the excitations in the gluon sector result in contributions to the properties of these states, which cannot come from just the quarks.

Studying the potentials of such exotic states can give a better understanding of their properties and existence, as well as help determine their masses which will be essential for the experimental study of these states. In experimental physics, the study of exotic matter is currently a popular topic, and a goal of the PANDA experiment at FAIR is the search of such exotic matter in the form of glueballs and hybrid mesons. A detailed understanding of these states will further improve our understanding of the strong interaction, and will serve as a test of the correctness of the standard model of particle physics at low energies.

The aim of this work is to expand on previous work in the study of hybrid static potentials, such as a first considerations of these in SU(2) gauge theory [25], and earlier works which show results for hybrid static potentials but do not show the details how these were obtained, such as [10]. Static potentials are computed by considering quarks with infinite masses, which approximate physical states of heavy quarks like $b\bar{b}$. We present the methods we use to construct trial states in SU(3) Yang-Mills theory, compute the relevant correlators, and analyze the data coming from statistical simulations on the lattice. We show first results for the hybrid static potentials of all states up to angular momentum $L = 2$, which are $\Sigma_g^+, \Sigma_g^-, \Sigma_u^+, \Sigma_u^-, \Pi_u, \Pi_g, \Delta_u, \Delta_g$ and examine the suitability of our trial states which are constructed using different structures and discuss possibilities how even better trial states might be obtained to further reduce statistical errors.

2 Theory

As mentioned, one method to calculate observables in QCD is to discretize space-time and perform direct numerical computations of correlators on this lattice of space-time points with the help of statistical Monte-Carlo simulations. To evaluate a path integral to compute these correlators, a large collection of field configurations is generated with a probability distribution that simulates the weight factor of the path integral. Correlators can then be computed by averaging their corresponding expressions on the lattice over these configurations. To make these computations possible, one has to remove the periodicity of the integrand in the path integral. This is achieved by the so called Wick-rotation of time $t \to -i\tau$ to complex values, with the euclidian time $\tau \in \mathbb{R}$. The resulting space-time metric is called the euclidian metric, and the integrand of the path integral decays exponentially over time in this metric, allowing the aforementioned computations. All expressions in this work are to be understood in this euclidian metric with euclidian time t.

2.1 Static potentials on the lattice

2.1.1 Definition of the static potential

Our aim in this work is to compute special types of potentials of quark antiquark pairs. We define the potential of the quark antiquark pair at a distance r to be the energy difference between the lowest energy state in QCD containing a quark antiquark pair $q\bar{q}$ and the vacuum state. To properly define the distance between the quarks and to prevent a decay or annihilation of the $q\bar{q}$ state, we take the quarks to have an infinite mass to localize them at fixed positions. We call this potential the static quark antiquark potential. To compute the static potential, we have to compute the correlator

$$C(t) = \langle\Omega|\, \mathcal{O}^\dagger(t)\mathcal{O}(0)\, |\Omega\rangle \tag{2.1}$$

for an operator $\mathcal{O}$ which is chosen in a way, so a trial state with the same quantum numbers as the state of interest is created, by acting $\mathcal{O}$ on the vacuum $|\Omega\rangle$. Inserting a set of energy eigenstates to the Hamilton operator $H\,|n\rangle = E_n\,|n\rangle$ and using the euclidian time translated operator $\mathcal{O}^\dagger(t) = e^{Ht}\mathcal{O}^\dagger(0)e^{-Ht}$, one finds

$$\begin{aligned} C(t) &= \sum_n \langle\Omega|\, e^{Ht}\mathcal{O}^\dagger(0)e^{-Ht}\, |n\rangle\, \langle n|\, \mathcal{O}(0)\, |\Omega\rangle \\ &= \sum_n |\langle n|\, \mathcal{O}(0)\, |\Omega\rangle|^2 e^{-(E_n - E_\Omega)t}. \end{aligned} \tag{2.2}$$

In the limit of large $t \to \infty$, we notice only the state of lowest energy $|0\rangle$ survives

$$\lim_{t\to\infty} C(t) \propto e^{-(E_0 - E_\Omega)t}. \tag{2.3}$$

To extract the static potential at distance r, which we defined to be the difference $E_0 - E_\Omega = V(r)$, we can fit an exponential function to the correlation function $C(t)$ at

large t, or fit a constant to the so called effective Potential

$$V_{\text{eff}}(t) = \frac{1}{a} \ln \left(\frac{C(t)}{C(t+a)} \right), \quad \text{with lattice spacing } a \tag{2.4}$$

at large t, which is more commonly used and will be the method we use in this work. Inserting (2.4) into (2.3), we identify the static potential with the effective potential at large t:

$$V(r) = \lim_{t \to \infty} V_{\text{eff}}(t). \tag{2.5}$$

2.1.2 Obtaining the static potential using lattice simulations

To compute the static potential on the lattice, we have to compute the path integral

$$C(t) = \frac{1}{Z} \int \mathcal{D}[A]\mathcal{D}[q,\overline{q}]\mathcal{O}^{\dagger}(t)\mathcal{O}(0)e^{-S[A,q,\overline{q}]} \tag{2.6}$$

where $S[A_\mu, q, \overline{q}]$ is the QCD action and $\mathcal{D}[A]\mathcal{D}[q,\overline{q}]$ denotes an integration over all possible quark- and gauge-field configurations. As mentioned before, this is done by averaging $C(t)$ over many configurations, which are generated using a heatbath algorithm, with a probability distribution that simulates the exponential weight factor in the path integral, which depends on the QCD action. To make this possible, we need a lattice expression of the correlator $C(t)$ and the QCD action S. However, since we are working with static quarks, the part of the QCD action which describes fermion dynamics is not needed, so we only need a lattice expression of the gauge, or gluon part S_g of the QCD action. In the continuum, the gluon action reads

$$S_g[A] = \frac{1}{2g^2} \int d^4x \, Tr \left[F_{\mu\nu}(x) F_{\mu\nu}(x) \right] \tag{2.7}$$

where $F_{\mu\nu}$ is the field strength tensor of the SU(3)-color gauge group and the trace is taken over color indices. The action S_g is invariant under the SU(3)-color gauge transformations, this symmetry must of course also be true for the corresponding lattice expression of S_g. On the lattice, the SU(3)-color gauge transformation is realized by choosing a set of SU(3) elements $\Omega(n)$, one for each lattice site n. The gauge transformation of the field A_μ then reads

$$A_\mu(n) \to A'_\mu(n) = \Omega(n) A_\mu(n) \Omega^{\dagger}(n) + i(\partial_\mu \Omega(n)) \Omega^{\dagger}(n). \tag{2.8}$$

To keep the invariance under SU(3)-color gauge transformations on the lattice, one has to introduce a set of oriented so called lattice link variables $U_\mu(n)$ with direction μ at lattice site n, as elements of the SU(3)-color gauge group, which are related to the gauge field A_μ via the relation

$$U_\mu(n) = e^{iaA_\mu(n)} \tag{2.9}$$

and transform under gauge transformations as

$$U_\mu(n) \to U'_\mu(n) = \Omega(n) U_\mu(n) \Omega^{\dagger}(n + ae_\mu), \tag{2.10}$$

with unit vectors e_μ. Link variables with opposite orientation are defined by

$$U_{-\mu}(n) = U_\mu^\dagger(n - ae_\mu). \tag{2.11}$$

One can show that the trace of a product of link variables along a closed loop is a gauge invariant object, which can be used to construct lattice expressions of the QCD gluon action S_g and physical observables. One possible definition of the lattice gauge action, the so called Wilson plaquette action is given by

$$S_g[U] = \frac{\beta}{3} \sum_n \sum_{\mu<\nu} \mathrm{Re}\left\{\mathrm{Tr}\left[\mathbb{1} - U_{\mu\nu}(n)\right]\right\}, \tag{2.12}$$

with the shortest possible loop of link variables, the so called plaquette, which is defined by

$$U_{\mu\nu}(n) = U_\mu(n)\, U_\nu(n + ae_\mu)\, U_{-\mu}(n + ae_\mu + ae_\nu)\, U_{-\nu}(n + ae_\nu). \tag{2.13}$$

The commonly used factor $\beta = 6/g^2$, where g is the coupling strength of the gauge fields to the quarks, is called *inverse coupling* and will be used as a parameter to set the lattice scale in our numerical simulations later on. Finally, one can verify that $S_g[U]$ reduces to the continuum gauge action in the continuum limit $a \to 0$:

$$\lim_{a\to 0} S_g[U] = S_g[A]. \tag{2.14}$$

With this lattice gauge action $S_g[U]$, a heatbath algorithm can be defined to generate gauge configurations, with each configuration being a set of link variables $U_\mu(n)$ for each direction $\mu \in \{t, x, y, z\}$ and every lattice site n.

To complete the computation of the static potential on the lattice, we need a lattice expression of the correlator $C(t)$. As pointed out before, each closed loop of link variables represents a physical observable. A special type of loop of this kind can be defined as a product of spatial paths

$$S(\mathbf{n}, \mathbf{m}, t) = U_{k_0}((\mathbf{n}, t))U_{k_1}((\mathbf{n} + a\mathbf{e}_{k_0}, t)) \ldots U_{k_N}((\mathbf{m} - a\mathbf{e}_{k_N}, t)) \tag{2.15}$$

connecting the lattice sites $(\mathbf{n}, t)$ and $(\mathbf{m}, t)$, which are called *Wilson lines*, and temporal paths

$$T(t_0, t_1, \mathbf{n}) = U_t((\mathbf{n}, t_0))U_t((\mathbf{n}, t_0 + a)) \ldots U_t((\mathbf{n}, t_1 - a)) \tag{2.16}$$

connecting the lattice sites $(\mathbf{n}, t_0)$ and $(\mathbf{n}, t_1)$. The so called *Wilson loop* is defined as the trace of the product of paths of this type:

$$W(|\mathbf{m} - \mathbf{n}|, t_1 - t_0) = \mathrm{Tr}\left[S(\mathbf{n}, \mathbf{m}, t_0)T(t_0, t_1, \mathbf{m})S^\dagger(\mathbf{n}, \mathbf{m}, t_1)T^\dagger(t_0, t_1, \mathbf{n})\right]. \tag{2.17}$$

In temporal gauge, where the temporal paths of the Wilson loop are the identity operator, one can show, that the expectation value of a Wilson loop is the correlator of its two Wilson lines (cf. [7]), which behaves just like the correlator (2.1). The trial states, which are created by the operators in this correlator, are also states containing a quark and

antiquark at positions $\mathbf{n}$ and $\mathbf{m}$. Thus, we can extract the static potential by fitting a constant to the effective potential (2.4) at large time separations $|t_1 - t_0| \to \infty$, where we compute the effective potential on the lattice using expectation values of Wilson loops in place of correlators $C(t)$:

$$V_{\text{eff}}(R,t) = \frac{1}{a} \ln\left(\frac{\langle W(R,t)\rangle}{\langle W(R,t+a)\rangle}\right), \quad \text{with lattice spacing } a. \tag{2.18}$$

2.1.3 Sommer parameter and lattice scale

To relate results of lattice simulations to physical quantities, the lattice spacing a has to be determined. One method to obtain the lattice spacing is based on the so called *Sommer parameter* r_0, which is defined via the force $F(r) = dV(r)/dr$ between the two static quarks of our static quark antiquark pair (cf. [7]). For the ordinary static quark potential, one can compare a lattice observable with experimental data to find that the quantity

$$F(r_0)r_0^2 = 1.65 \tag{2.19}$$

corresponds to a Sommer parameter of $r_0 \approx 0.5\,\text{fm}$. Although other, more precise methods to determine the lattice spacing exist, in this work, we determine the lattice spacing using the Sommer parameter $r_0 = 0.5\,\text{fm}$. For the ordinary static potential, a parametrization $V(r) = A + \frac{B}{r} + \sigma r$ of the static potential is known, for which the force is

$$F(r) = \frac{d}{dr}V(r) = -\frac{B}{r^2} + \sigma. \tag{2.20}$$

Fitting the parametrized form of the potential to our numerical data $aV(an)$ of the potential, with $r = an$, we obtain the dimensionless fit parameters B and $\hat{\sigma} = \sigma a^2$. Comparing the definition of the Sommer parameter (2.19) to the expression for the force for the parametrized potential, we obtain the lattice spacing as a function of these dimensionless fit parameters

$$a = 0.5 \cdot \sqrt{\frac{\hat{\sigma}}{1.65 + B}}\,\text{fm}. \tag{2.21}$$

2.2 Hybrid states and quantum numbers

A hybrid static potential is a static potential of a quark antiquark pair with additional contributions to its quantum numbers, which come from the gluon excitations. We saw in the previous section, that static potentials on the lattice are obtained by computing Wilson loops and that the states in the resulting correlators describe quark antiquark pairs located at fixed spatial positions. The choice of the shape of the Wilson lines in the Wilson loop then determines the quantum numbers of the corresponding quark antiquark state. Choosing the Wilson lines as straight paths of links along the quark antiquark pair separation axis produces the regular static potential, with quantum numbers that are determined by just the structure of the quark antiquark pair.

It is however also possible to choose different kinds of Wilson lines, which are not just straight paths of links. This will result in states that have additional contributions to their quantum numbers, which come from gluon excitations, since the structure of the resulting states is defined by the shape of the Wilson lines, which are products of elements of the SU(3)-color gauge group. We call the part of the Wilson line, which is not a straight path of links along the separation axis an '*insertion*'. Potentials for states of this type are called *hybrid static potentials*. In this section, we will see that the quantum numbers of these states are:

- Angular momentum with respect to the quark antiquark pair separation axis 'L'. In this work, we use $|L|$
- A quantum number Q_{PC} corresponding to the combination of parity and charge conjugation '$\mathcal{P} \circ \mathcal{C}$'.
- An additional quantum number 'P_x' corresponding to the spatial inversion along a coordinate axis perpendicular to the quark antiquark pair separation axis.

Our notation in this work will be of the format $L^{P_x}_{Q_{PC}}$, where $L \in \{\Sigma, \Pi, \Delta\}$ for $L = 0, 1, 2$ respectively, $Q_{PC} \in \{g, u\}$ for $Q_{PC} = +(g), -(u)$, and $P_x \in \{+, -\}$.

In this section we will often use the term '*path of links*', which we define to be a product of links, where the startpoint of each link in the product is equal to the endpoint of the previous link in the product, such that we can visualize the product as an oriented continuous path between two lattice sites. We call

$$\mathcal{S} = \prod_{j=0}^{N} U_{i_j}(n_j) = U_{i_0}(n_0)\, U_{i_1}(n_1) \dots U_{i_N}(n_N) \tag{2.22}$$

a *path of links* with some startpoint n_0 if and only if $n_k = n_{k-1} + a e_{i_{k-1}}$ for all $k = 1, 2, \dots, N$, where n_N is called the endpoint, a is the lattice spacing and $i_0, \dots, i_N \in \{\pm x, \pm y, \pm z\}$ (with $e_{-j} = -e_j$) define the shape and orientation of the path on the lattice.

2.2.1 Angular momentum

To determine a given trial states quantum numbers, consider some state $|H\rangle$ with defined angular momentum L. In the continuum, the state reads

$$|H\rangle = \int_0^{2\pi} \mathrm{d}\varphi\, Y_L(\varphi)\, \mathcal{O}(\varphi)\ |\Omega\rangle\,, \tag{2.23}$$

where $\mathcal{O}(\varphi)$ is some operator depending on an angle φ with respect to the separation axis of the quark antiquark pair, and $Y_L(\varphi) = \exp(iL\varphi)$ is an analog to spherical harmonics with respect to the separation axis for a state with angular momentum L. Let $\hat{R}(\varphi)$ be

the rotation operator about an angle φ around the separation axis. Rotating the state $|H\rangle$ yields

$$\begin{aligned} |H\rangle \xrightarrow{\hat{R}(\varphi)} & \int_0^{2\pi} \mathrm{d}\varphi' \, Y_L(\varphi') \left(\hat{R}(\varphi)\, \mathcal{O}(\varphi')\right) |\Omega\rangle = \int_0^{2\pi} \mathrm{d}\varphi' \, Y_L(\varphi')\, \mathcal{O}(\varphi' + \varphi) \, |\Omega\rangle \\ &= \int_0^{2\pi} \mathrm{d}\varphi'' \, Y_L(\varphi'' - \varphi)\, \mathcal{O}(\varphi'') \, |\Omega\rangle = e^{-iL\varphi} \int_0^{2\pi} \mathrm{d}\varphi'' \, Y_L(\varphi'')\, \mathcal{O}(\varphi'') \, |\Omega\rangle \\ &= e^{-iL\varphi} \, |H\rangle \,, \end{aligned} \tag{2.24}$$

using the 2π-periodicity of $Y_L(\varphi)$ and $\mathcal{O}(\varphi)$. We can also express the rotation operator as an element of the rotation group:

$$|H\rangle \xrightarrow{\hat{R}(\varphi)} e^{-i\hat{L}\varphi} \, |H\rangle \,, \tag{2.25}$$

where $\hat{L}$ is the angular momentum operator with respect to the separation axis. Comparing equations (2.24) and (2.25), we identify that the constructed state has angular momentum L:

$$\hat{L} \, |H\rangle = L \, |H\rangle \,. \tag{2.26}$$

On the lattice, instead of an integration, we have a sum over different values of φ, which means that an operator $\mathcal{O}(\varphi)$ has to be constructed in a similar way for each value of φ using link variables, so that a 2π-periodicity is still given. In this work, we only use nearest neighbor lattice sites, so we only consider the angles $\varphi = 0, \pi/2, \pi, 3\pi/2$, for which an operator does not change its shape after a rotation, i.e. $\hat{R}((4-n)\pi/2)\mathcal{O}(n\pi/2) = \mathcal{O}(0), \forall n \in \mathbb{Z}$. To obtain trial states for angular momenta $L = 0, 1, 2$, we simply have to build the sum

$$|H\rangle = \sum_{k=0}^{3} e^{iLk\frac{\pi}{2}} \, \mathcal{O}\left(k\frac{\pi}{2}\right) |\Omega\rangle \tag{2.27}$$

and substitute the desired $L = 0, 1, 2$. Since the state is realized on the lattice by computing Wilson loops with insertions I, the only part of the operator $\mathcal{O}(\varphi)$ that is dependent on the angle φ are these insertions, so we first consider a sum using only insertions, instead of the full operators (i.e. we build a sum like (2.27) for $\mathcal{O} = I$). The full operators are then constructed from these expressions in the following sections.

In practice, we choose a particular path of links as insertion I (e.g. Fig. 2.1a), and rotate this path by the angles $\varphi = 0, \pi/2, \pi, 3\pi/2$ around the quark antiquark pair separation axis to obtain the four rotations $I(n\pi/2) = \hat{R}(n\pi/2)I, \; n = 0, 1, 2, 3$ of this path (Fig. 2.1b), which contribute to the desired trial state. To obtain the needed expressions for defined angular momentum, we then build the sum of these four rotations, by substituting the desired L into equation (2.27) and using $\mathcal{O} = I$.
For $L = 0$, we obtain from Eq. (2.27) the factor 1 for each angle, so we simply sum over all rotations of the insertion I with coefficients 1 to obtain a sum S_0 which is the φ-dependent part of an operator, which we can use to construct a trial state with angular momentum $L = 0$:

$$S_0(I) = \left(1 + \hat{R}\left(\frac{\pi}{2}\right) + \hat{R}(\pi) + \hat{R}\left(\frac{3\pi}{2}\right)\right) I \tag{2.28}$$

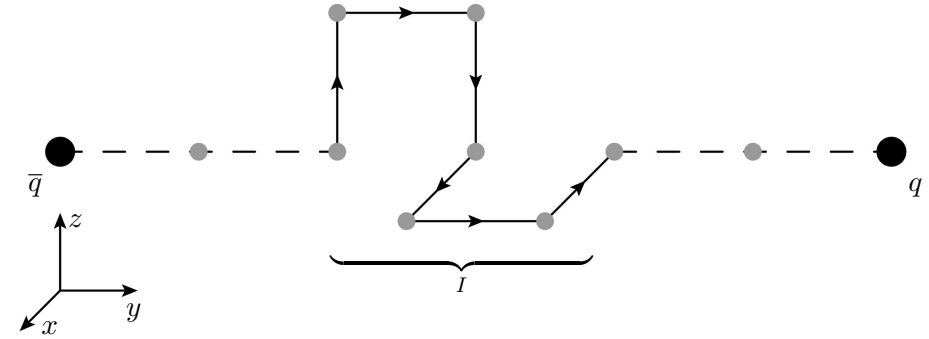

(a) Example for an insertion I (continuous line) placed on the midpoint of the quark antiquark pair separation axis (dashed line). Grey dots indicate lattice sites.

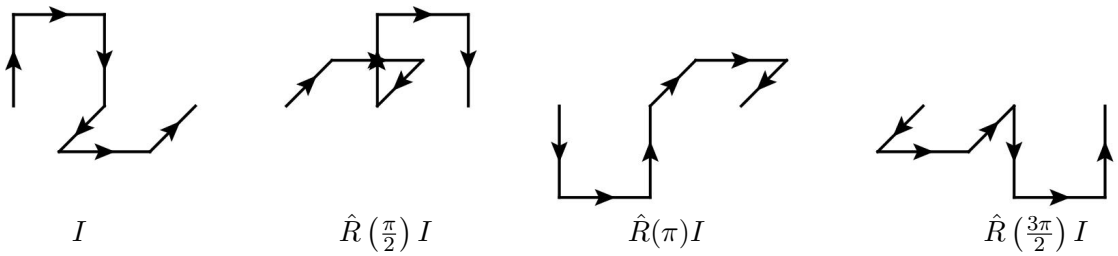

(b) Possible rotations of the spatial path I, considering only links between nearest neighbor lattice sites.

Figure 2.1: Example for an insertion (a), and its rotations (b).

In the same manner, we obtain the factors $1, -1, 1, -1$ for angular momentum $L = \pm 2$ for the angles $0, \pi/2, \pi, 3\pi/2$ respectively. An operator for $|L| = 2$ is then

$$S_2(I) = \left(1 - \hat{R}\left(\frac{\pi}{2}\right) + \hat{R}(\pi) - \hat{R}\left(\frac{3\pi}{2}\right)\right) I. \tag{2.29}$$

Finally, for $L = \pm 1$, we obtain two different operators:

$$\begin{aligned} S_{+1}(I) &= \left(1 + i\hat{R}\left(\frac{\pi}{2}\right) - \hat{R}(\pi) - i\hat{R}\left(\frac{3\pi}{2}\right)\right) I, \\ S_{-1}(I) &= \left(1 - i\hat{R}\left(\frac{\pi}{2}\right) - \hat{R}(\pi) + i\hat{R}\left(\frac{3\pi}{2}\right)\right) I. \end{aligned} \tag{2.30}$$

To simplify computations in this work, we instead use the combination

$$S_1(I) = \frac{1}{2}\left(S_{+1} + S_{-1}\right) = \left(1 - \hat{R}(\pi)\right) I, \tag{2.31}$$

which is used to construct a trial state with angular momentum $|L| = 1$.

Note that states which are constructed using the operators S_0, S_1, S_2 will not represent the exact states for angular momenta $|L| = 0, 1, 2$, but will also have overlap with sectors

of higher angular momentum, because we did not include next-to-nearest neighbor or farther lattice sites in our considerations. In general, since we are restricted to a lattice, it is not possible to fully remove overlaps with states of higher angular momentum with a finite lattice size due to being restricted to a finite amount of rotations.

2.2.2 Parity and charge conjugation

Analog to the previous section, to determine the parity and charge conjugation quantum number, we will apply these transformations to a trial state. Without loss of generality, we place the quark and antiquark on the z-axis at the locations $\mathbf{r}_q = (0, 0, R)$ for the quark q, and $\mathbf{r}_{\overline{q}} = (0, 0, -R)$ for the antiquark $\overline{q}$. Furthermore, the time coordinate is fixed, so only the z-coordinate is written explicitly in this section. We call the midpoint on the quark antiquark pair separation axis M. To simplify some calculations, we introduce an additional notation for lattice links:

$$U_{\pm z}(n) = U(R_0, R_0 \pm a), \tag{2.32}$$

for a lattice site $n = (t, 0, 0, R_0)$. With this notation, we define a path of links along the quark antiquark pair separation axis

$$\mathcal{U}(R_0, R_1) = \prod_{j=0}^{|R_1 - R_0|/a - 1} U(R_0 + ja \cdot \mathrm{sgn}(R_1 - R_0), R_0 + (j+1)a \cdot \mathrm{sgn}(R_1 - R_0)). \tag{2.33}$$

From the discretization of the gauge action, we know that we can write the lattice links $U_\mu(n)$ in terms of the continuum gauge fields A_μ:

$$U_\mu(n) = e^{iaA_\mu(n)}. \tag{2.34}$$

Furthermore, the behavior of $A_\mu(n)$ under charge conjugation is known:

$$A_\mu(n) \xrightarrow{\mathcal{C}} -A_\mu^T(n). \tag{2.35}$$

The behavior of a lattice link under charge conjugation is then

$$\begin{aligned} U_\mu(n) \xrightarrow{\mathcal{C}} U_{\mu,\mathcal{C}}(n) = e^{-iaA_\mu^T(n)} &= \left[e^{-iaA_\mu(n)}\right]^T \overset{(*)}{=} \left[e^{-iaA_\mu^\dagger(n)}\right]^T \\ &= \left[U_\mu^\dagger(n)\right]^T = U_{-\mu}^T(n + ae_\mu), \end{aligned} \tag{2.36}$$

where we used the hermiticity of A_μ in step $(*)$ and the definition of opposite oriented links in the last step. The charge conjugated link is the transpose of the original link with reversed direction.
The final object we need to construct a trial state, is some spatial path of links $I(-d, d)$ (e.g. the one shown in Fig. 2.1a) which we will use as insertion in the Wilson loop:

$$I(-d, d) = U_{i_1}(-de_z)U_{i_2}(-de_z + ae_{i_1}) \dots U_{i_n}(de_z - ae_{i_n}), \tag{2.37}$$

with $i_1, \ldots, i_n \in \{\pm x, \pm y, \pm z\}$ (with $e_{-i} = -e_i$) and some distance d from the midpoint M. The trial state then reads

$$|H\rangle = \overline{q}(-R)\,\mathcal{U}(-R,-d)\,I(-d,d)\,\mathcal{U}(d,R)\,q(R)\,|\Omega\rangle\,, \tag{2.38}$$

where $|\Omega\rangle$ is the vacuum state. Furthermore, we also need the behavior of the quarks under parity and charge conjugation, which read

$$q(R) \xrightarrow{\mathcal{P}} \gamma^0 q(-R) \tag{2.39}$$

$$\overline{q}(R) \xrightarrow{\mathcal{P}} \overline{q}(-R)\gamma^0 \tag{2.40}$$

$$q(R) \xrightarrow{\mathcal{C}} C\,\overline{q}^T(R) \tag{2.41}$$

$$\overline{q}(R) \xrightarrow{\mathcal{C}} q^T(R)C, \tag{2.42}$$

where $C = -C^T = -C^{-1}$ is the charge conjugation operator. Applying parity transformation and charge conjugation to $|H\rangle$ yields

$$\begin{aligned}
\mathcal{P}\circ\mathcal{C}\,|H\rangle &= \mathcal{C}\left[\overline{q}(R)\,\gamma^0\,\mathcal{U}(R,d)\,I_{\mathcal{P}}(-d,d)\,\mathcal{U}(-d,-R)\,\gamma^0\,q(-R)\right]|\Omega\rangle \\
&= q^T(R)\,C\,\mathcal{U}_{\mathcal{C}}(R,d)\,I_{\mathcal{P},\mathcal{C}}(-d,d)\,\mathcal{U}_{\mathcal{C}}(-d,-R)\,C\,\overline{q}^T(-R)\,|\Omega\rangle \\
&= (-)^2\,\overline{q}(-R)\,\mathcal{U}_{\mathcal{C}}^T(-d,-R)\,I_{\mathcal{P},\mathcal{C}}^T(-d,d)\,\mathcal{U}_{\mathcal{C}}^T(R,d)q(R)\,|\Omega\rangle\,,
\end{aligned} \tag{2.43}$$

where we used $\left(\gamma^0\right)^2 = 1$ in the second step and $C^2 = -1$ and the fact that q and $\overline{q}$ anticommutate in the second step. The remaining expressions to evaluate are $\mathcal{U}_{\mathcal{C}}^T$ and $I_{\mathcal{P},\mathcal{C}}^T$. First we evaluate $\mathcal{U}_{\mathcal{C}}^T$:

$$\begin{aligned}
\mathcal{U}_{\mathcal{C}}^T(R_0,R_1) &= \Bigg[\prod_{j=0}^{|R_1-R_0|/a-1} \mathcal{U}_{\mathcal{C}}(R_0 + ja\cdot\mathrm{sgn}(R_1-R_0), \\
&\qquad\qquad R_0 + (j+1)a\cdot\mathrm{sgn}(R_1-R_0))\Bigg]^T \\
&= \Bigg[\prod_{j=0}^{|R_1-R_0|/a-1} \mathcal{U}^T(R_0 + (j+1)a\cdot\mathrm{sgn}(R_1-R_0), \\
&\qquad\qquad R_0 + ja\cdot\mathrm{sgn}(R_1-R_0))\Bigg]^T \\
&\overset{(*)}{=} \prod_{l=0}^{|R_1-R_0|/a-1} \mathcal{U}(R_1 + la\cdot\mathrm{sgn}(R_0-R_1), \\
&\qquad\qquad R_1 + (l+1)a\cdot\mathrm{sgn}(R_0-R_1)) \\
&= \mathcal{U}(R_1,R_0),
\end{aligned} \tag{2.44}$$

where in step $(*)$, we substituted $j = |R_1 - R_0|/a - 1 - l$ to transpose the product, which reverses its factors. After charge conjugating, each link is transposed and its direction

is reversed according to (2.36). The order of links is then reversed by the additional transposition which comes from the transformation of the trial state as shown by (2.43). The final expression is again a path of links along the separation axis, but with reversed direction, so that the parity transformed charge conjugated trial state reads

$$\mathcal{P} \circ \mathcal{C} \, |H\rangle = \overline{q}(-R)\, \mathcal{U}(-R,-d)\, I^T_{\mathcal{P},\mathcal{C}}(-d,d)\, \mathcal{U}(d,R)\, q(R)\, |\Omega\rangle \, . \tag{2.45}$$

To identify a quantum number Q_{PC} corresponding to $\mathcal{P} \circ \mathcal{C}$ transformation, we require

$$\mathcal{P} \circ \mathcal{C} \, |H\rangle = Q_{PC} \, |H\rangle \, . \tag{2.46}$$

To fulfill this relation, we compare (2.38) to (2.45) and see that we must have

$$I^T_{\mathcal{P},\mathcal{C}}(-d,d) = Q_{PC}\, I(-d,d), \tag{2.47}$$

i.e. applying the given transformation to the insertion in the Wilson loop must reproduce that insertion up to a factor Q_{PC}, which is precisely the quantum number of the hybrid state corresponding to $\mathcal{P}\circ\mathcal{C}$ transformation. Evaluating $I^T_{\mathcal{P},\mathcal{C}}(-d,d)$ is more complicated, but can be visualized with arguments already made above (cf. Fig. 2.2).
First, the parity transformation $\mathcal{P}$ reflects each point on the path of links $I(-d,d)$ on the midpoint M, so the result is again a path of links. Start- and endpoint of $I(-d,d)$ lie on the separation axis, so they are simply flipped by the parity transformation. We can write

$$\begin{aligned} I(-d,d) \xrightarrow{\mathcal{P}} I_{\mathcal{P}}(-d,d) &= I'(d,-d) \\ &= U_{-i_1}(de_k) U_{-i_2}(de_k - ae_{i_1}) \ldots U_{-i_n}(-de_k + ae_{i_n}). \end{aligned} \tag{2.48}$$

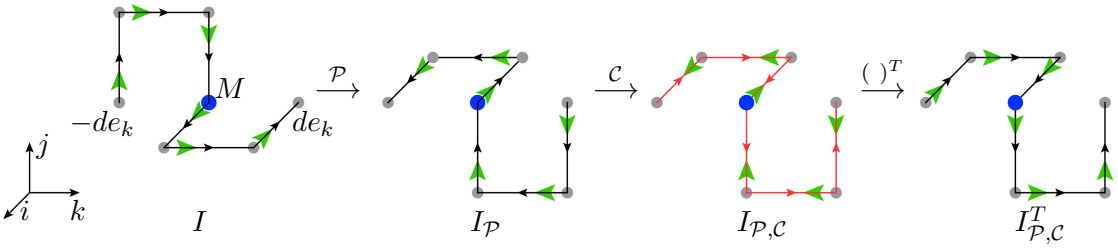

Figure 2.2: Visualizing the evaluation of $I^T_{\mathcal{P},\mathcal{C}}$ for an exemplary path, first applying a parity transformation $\mathcal{P}$, then charge conjugation $\mathcal{C}$, and finally transposing $(\,)^T$. The quark antiquark pair separation axis lies on the k-axis, its midpoint M (blue dot) is the origin. Oriented black lines indicate link variables in the corresponding direction between lattice sites (grey dots). Red colored lines indicate transposed link variables, and green arrows indicate the order in which link variables are multiplied to build the final product.

Charge conjugating $I'(d,-d)$, reverses the direction of all links once again and transposes each link, as we have seen (Eq. (2.36)). Evaluating the final transposition then reorders

the reversed links to form another path of links with the same start- and endpoints as the untransformed path of links $I(-d,d)$, analog to (2.44). In conclusion, we obtain the fully transformed insertion $I^T_{\mathcal{P},\mathcal{C}}(-d,d)$, by simply reflecting the original path of the insertion $I(-d,d)$ on the midpoint M and then reversing the resulting paths direction, such that start and endpoints are not changed:

$$I^T_{\mathcal{P},\mathcal{C}}(-d,d) = I'(-d,d) = U_{i_n}(-de_k)U_{i_{n-1}}(-de_k + ae_{i_n})\dots U_{i_1}(de_k - ae_{i_1}). \tag{2.49}$$

Plugging (2.49) into equation (2.47), we obtain the condition

$$I'(-d,d) = Q_{PC}\, I(-d,d) \tag{2.50}$$

to construct a trial state with a defined $\mathcal{P}\circ\mathcal{C}$ quantum number. In general, it is not possible to fulfill this condition if I is just a single path of links. Instead, we must take a sum

$$S_{\mathcal{I}}(-d,d) = \sum_j w_j I_j(-d,d) \tag{2.51}$$

over a set of paths $\mathcal{I} = \{I_j(-d,d)\}$ with weights w_j, which transform into each other when applying $\mathcal{P}\circ\mathcal{C}$ transformation, such that $S_{\mathcal{I}}$ fulfills the condition (2.50):

$$S'_{\mathcal{I}}(-d,d) = \sum_j w_j I'_j(-d,d) = Q_{PC}\, S_{\mathcal{I}}(-d,d). \tag{2.52}$$

Possible values for the quantum number are $Q_{PC} = \pm 1$, because applying $\mathcal{P}\circ\mathcal{C}$ transformation twice means reflecting each insertion in the sum twice on the separation axis, which will return the original sum, such that $(\mathcal{P}\circ\mathcal{C})^2\,|H\rangle = Q^2_{PC}\,|H\rangle = |H\rangle$. Later in this chapter, we will discuss a method to construct such a sum $S_{\mathcal{I}}(-d,d)$ from an arbitrary choice for the insertion in the Wilson loop.

2.2.3 P_x

Finally, the additional quantum number P_x can also be determined by applying its corresponding transformation to a trial state. This transformation is the spatial inversion along one coordinate axis perpendicular to the quark antiquark pair separation axis. Again w.l.o.g., we place quark q and antiquark $\overline{q}$ on the z-axis at positions $\mathbf{r}_q = (0,0,R)$ and $\mathbf{r}_{\overline{q}} = (0,0,-R)$ respectively. To determine P_x, the choice of coordinate system is arbitrary. However, in general, the inversion of the x-axis can produce a different factor for both choices, which means there are two orthogonal states in this case. Due to the arbitrary choice of a coordinate system however, we cannot assign a unique P_x to the given state in this case. Thus both possible choices of coordinate system have to be checked, and a unique quantum number P_x can only be identified, if both choices have the same effect. Using the definitions for $I(R_0,R_1)$,$\mathcal{U}(R_0,R_0)$ and trial state $|H\rangle$ from the previous section (Eq. (2.33), (2.37), (2.38)), we apply the spatial inversion $\mathcal{P}_x$ of the x-coordinate, for both possible choices of a coordinate system.

$$\begin{aligned}\mathcal{P}_x\,|H\rangle &= \mathcal{P}_x\,\overline{q}(-R)\,U(-R,d)\,I(-d,d)\,U(d,R)\,q(R)\,|H\rangle \\ &= \overline{q}(-R)\,U(-R,d)\;[\mathcal{P}_x\;I(-d,d)]\;U(d,R)\,q(R)\,|H\rangle\,.\end{aligned} \tag{2.53}$$

We immediately identify the condition

$$\mathcal{P}_x \, I(-d,d) = P_x \, I(-d,d). \tag{2.54}$$

To associate a unique quantum number P_x with the trial state, (2.54) must hold for both choices of the coordinate system. Like with the parity and charge conjugation quantum

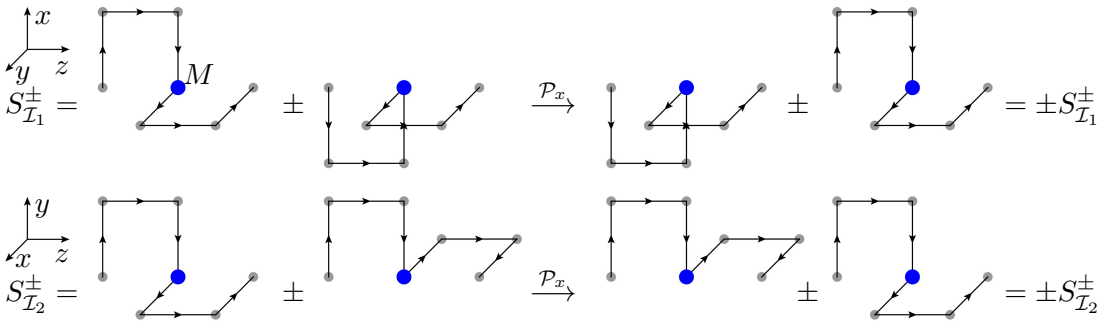

Figure 2.3: Application of $\mathcal{P}_x$ to exemplary sums of insertions for both possible coordinate systems with the quark antiquark pair located on the z-axis. The midpoint of the separation axis M (blue dot) lies on the origin. In both cases, applying the shown spatial inversion transforms the terms of the sum into each other, reproducing the sum up to a change in sign.

number, (2.54) can in general only be fulfilled, if instead of inserting a single path of links $I(-d,d)$, we insert a sum $S_{\mathcal{I}}(-d,d)$ over multiple paths as defined by (2.51) such that (cf. Fig. 2.3)

$$\mathcal{P}_x \, S_{\mathcal{I}}(-d,d) = P_x \, S_{\mathcal{I}}(-d,d). \tag{2.55}$$

Obviously, it is $\mathcal{P}_x^2 = 1$, such that possible values for the associated quantum number are $P_x = \pm 1$.

2.2.4 Construction of trial states

In this section, we show how to construct a trial state from any given single insertion I for the Wilson loop as defined by (2.37). This requires constructing a sum $S_{\mathcal{I}}$ as defined by (2.51) which satisfies both conditions (2.52) and (2.55) and choosing suitable weights w_j to obtain the desired quantum numbers L, Q_{PC} and P_x. First we choose an arbitrary shape for the insertion in the Wilson loop, by fixing the directions $i_1, \ldots, i_n \in \{\pm x, \pm y, \pm z\}$ in Eq. (2.37). This choice of insertion I is at first a guess, and in this work, we will compute effective potentials for different I and investigate the quality of the resulting effective potentials as well as evaluate the relative contributions of the trial states constructed with each I to the overlap with the energy eigenstates of interest. We now construct the sum $S_{\mathcal{I}}$ to choose a particular set of the quantum numbers L, Q_{PC}, P_x discussed in the previous sections. As we have seen in section 2.2.1, angular momentum L can be fixed by building one of the sums (2.28), (2.31) or (2.29), namely $S_{|L|}(I)$, for

angular momentum $L = 0$, $|L| = 1$ and $|L| = 2$ respectively. To obtain a final form of $S_{\mathcal{I}}$, we project the trial state created by the operator $S_{|L|}(I)$ onto the subspace of eigenstates to $\mathcal{P}_x$ and $\mathcal{P} \circ \mathcal{C}$ using the projection operators

$$\mathbb{P}_{P_x} = \frac{1}{2}(1 + P_x \mathcal{P}_x), \tag{2.56}$$

$$\mathbb{P}_{PC} = \frac{1}{2}(1 + Q_{PC} \mathcal{P} \circ \mathcal{C}), \tag{2.57}$$

so that our final operator which creates a trial state with the quantum numbers $|L|, Q_{PC}, P_x$ is

$$S_{\mathcal{I}} = \mathbb{P}_{P_x} \mathbb{P}_{PC} S_{|L|} = \mathcal{N}(1 + P_x \mathcal{P}_x + Q_{PC} \mathcal{P} \circ \mathcal{C} + P_x Q_{PC} \mathcal{P}_x \mathcal{P} \circ \mathcal{C}) S_{|L|}(I). \tag{2.58}$$

We quickly see that (2.58) fulfills conditions (2.52) and (2.55), due to

$$\mathcal{P}_x \, \mathbb{P}_{P_x} = \frac{1}{2}(\mathcal{P}_x + P_x) = \frac{P_x}{2}(1 + P_x \mathcal{P}_x) = P_x \, \mathbb{P}_{\mathcal{P}_x}, \tag{2.59}$$

$$\mathcal{P} \circ \mathcal{C} \, \mathbb{P}_{PC} = \frac{1}{2}(\mathcal{P} \circ \mathcal{C} + Q_{PC}) = \frac{Q_{PC}}{2}(1 + Q_{PC} \mathcal{P} \circ \mathcal{C}) = Q_{PC} \, \mathbb{P}_{PC}, \tag{2.60}$$

using that $P_x^2 = 1$ and $Q_{PC}^2 = 1$. Also, the normalization factor $\mathcal{N} = \frac{1}{4}$ in $S_{\mathcal{I}}$ can be dropped, as it has no impact on the computation of effective potentials. Note that for a given I, some choices of quantum numbers L, Q_{PC}, P_x can lead to $S_{\mathcal{I}} = 0$, indicating that a trial state with these quantum numbers cannot be constructed for this particular choice of I.

2.3 Choice of insertions and quantum numbers

In this section, we list our choice of insertions we used to compute hybrid static potentials in this work. The aim was to first investigate very simple paths to possibly identify which properties are better suited to construct trial states with larger overlap to the desired energy eigenstates. In addition, two insertions with more complicated paths are also investigated.

Fig. 2.4a shows our choice of insertions. I_0 has a length of one link along the separation axis, all other insertions span over the whole distance between quark and antiquark. In the case of an even numbered quark antiquark separation R, I_0 cannot be placed on the center of the separation axis, instead it can be placed on the nearest lattice site to the center, either in direction of the antiquark $\bar{q}$, or in direction of the quark q. We label these two possibilities $I_{0,L}$ and $I_{0,R}$ (cf. Fig. 2.4b). Computing a Wilson loop with either just $I_{0,L}$ or just $I_{0,R}$ would result in a trial state with different symmetry properties than I_0. Instead, we use the average over both possibilities

$$I_{0,\text{even}} = \frac{1}{2}(I_{0,L} + I_{0,R}) \tag{2.61}$$

as an insertion in the case of even R. $I_{0,\text{even}}$ has the same symmetry properties for even R, as I_0 does for odd R, so we obtain a trial state with the same quantum numbers in

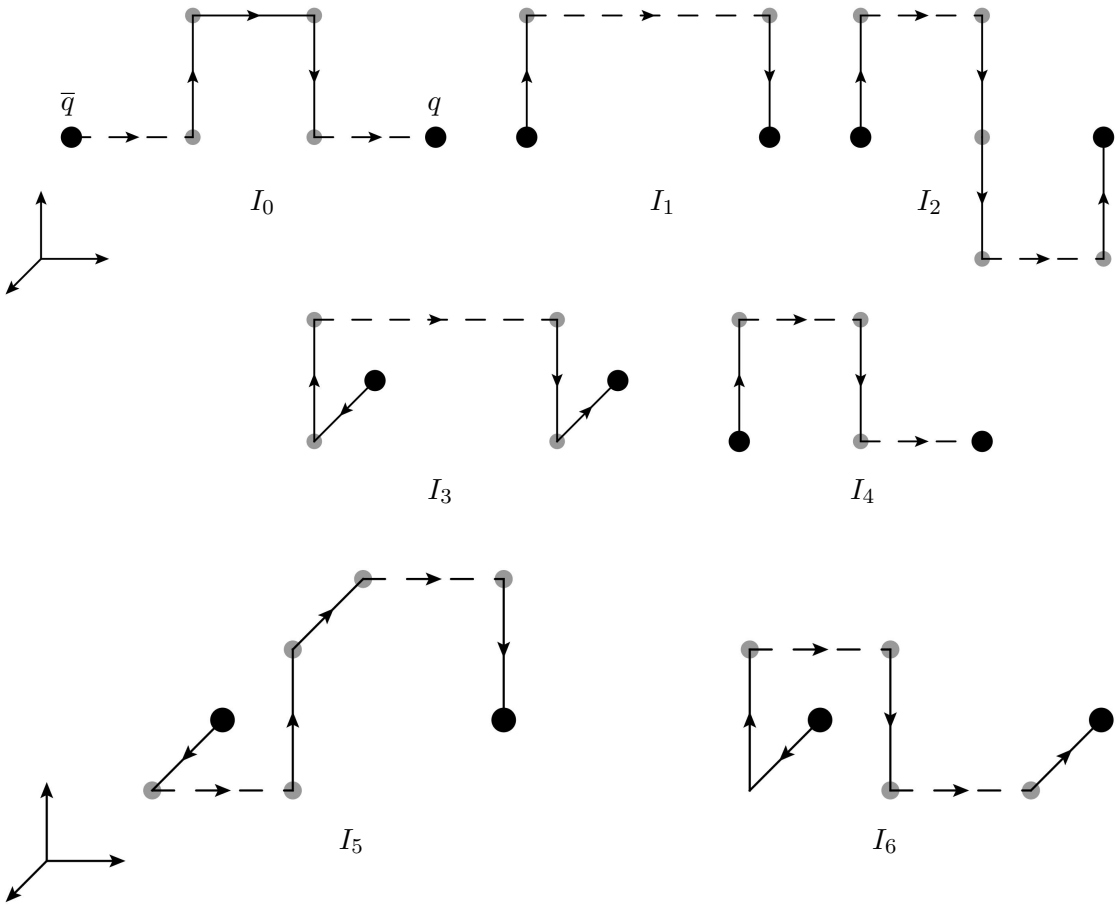

(a) Our choice of insertions $I_0, I_1, \ldots, I_6$. Black dots indicate quarks $\overline{q}, q$, separated by a distance Ra, grey dots indicate lattice sites. Continuous lines are single link variables, dashed lines represent a straight path of links of length $\frac{R}{2}$ for I_2, I_4, I_5, I_6 for even R, length $\frac{R-1}{2}$ for I_0 for odd R, and length R for I_1, I_3.

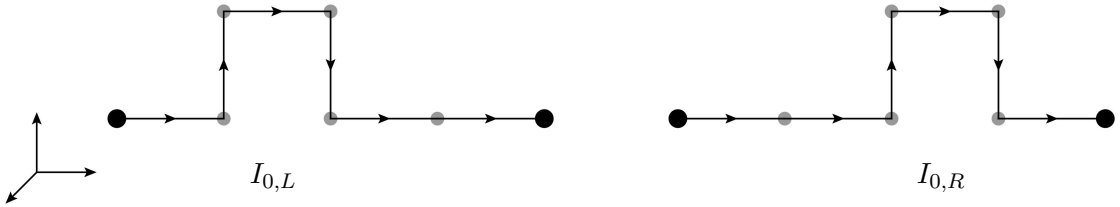

(b) Possibilities of placing insertion I_0 on the separation axis of a quark antiquark pair separated by an even distance $R = 4$.

Figure 2.4: An illustration of all insertions used in this work.

both cases. Likewise, for insertions I_2, I_4, I_5, I_6, in the case of odd R, we have the possibility to choose the left straight path (dashed line in Fig. 2.4a) to have length $\frac{R+1}{2}$ and the right straight path to have length $\frac{R-1}{2}$, or vice versa, and we choose the insertion for odd R to be the average over these possibilities.
Table 2.1 shows a list of possible trial states for each insertion (i.e. quantum numbers for which $S_{\mathcal{I}} \neq 0$).

Insertion	possible quantum numbers
$I_{0,1}$	$\Sigma_g^+, \Pi_u, \Delta_g^+$
I_2	$\Sigma_g^+, \Pi_g, \Delta_g^+$
I_3	$\Sigma_g^+, \Sigma_g^-, \Pi_u, \Delta_g^+, \Delta_g^-$
I_4	$\Sigma_g^+, \Sigma_u^+, \Pi_g, \Pi_u, \Delta_g^+, \Delta_u^+$
I_5	$\Sigma_g^+, \Sigma_u^-, \Pi_g, \Pi_u, \Delta_u^+, \Delta_g^-$
I_6	$\Sigma_g^+, \Sigma_u^+, \Sigma_g^-, \Sigma_u^-, \Pi_g, \Pi_u, \Delta_g^+, \Delta_u^+, \Delta_g^-, \Delta_u^-$

Table 2.1: List of possible trial states that can be constructed with each insertion.

2.3.1 Generation of numerical data and symmetry averaging

In this section, we give an outline how our numerical data was generated. As shown in the previous sections, we first choose an insertion I_j that we want to use to create the trial state. As a next step, we have to identify which kind of Wilson loops we have to compute to obtain the static potential for each desired set of quantum numbers. We have seen that a combination, which generates a trial state with defined quantum numbers, is given by (2.58). However, each term in this sum can be a different path on the lattice. All paths on the lattice we have to consider are given by applying the combinations of rotations and $\mathcal{P}_x$ and $\mathcal{P} \circ \mathcal{C}$ transformations as they appear in the sum (2.58). This can lead to up to sixteen different paths. One such maximal example is shown in figure 2.5.

Like in previous sections, we place the quark and antiquark a distance R away from the midpoint M of the separation axis, so their positions are $\mathbf{r}_q = \mathbf{M} + R\mathbf{e}_k$ and $\mathbf{r}_{\overline{q}} = \mathbf{M} - R\mathbf{e}_k$ respectively, where $\mathbf{M}$ is the spatial position of the midpoint. The Wilson loops we have to compute are given by expanding the sums $S_{\mathcal{I}}$ in the expression

$$\begin{aligned} C(I_j) = \mathrm{Tr}\big[&\mathcal{U}^{t_0}(-R,-d)\, S^{t_0}_{\mathcal{I}(I_j)}(-d,d)\, \mathcal{U}^{t_0}(d,R)\, T(t_0,t_1,\mathbf{r}_q) \\ &\Big\{\mathcal{U}^{t_1}(-R,-d)\, S^{t_1}_{\mathcal{I}(I_j)}(-d,d)\, \mathcal{U}^{t_1}(d,R)\Big\}^\dagger T^\dagger(t_0,t_1,\mathbf{r}_{\overline{q}})\big], \end{aligned} \tag{2.62}$$

where $\mathcal{U}^t(R_0,R_1)$ and $S^t_{\mathcal{I}}(-d,d)$ are as defined before (cf. (2.33), (2.58)), with an additional time index, indicating that all links in the product are at time t. For the insertion I_6, there are 16×16 Wilson loops to compute. To obtain the effective potential $V(2R, t_1 - t_0)$ from the numerical simulations, we compute the average of each of these Wilson loops over each lattice site (effectively averaging over each midpoint M and each t_0 with $t_1 = t_0 + \delta t$ for fixed R and δt) and each configuration. Additionally, we average

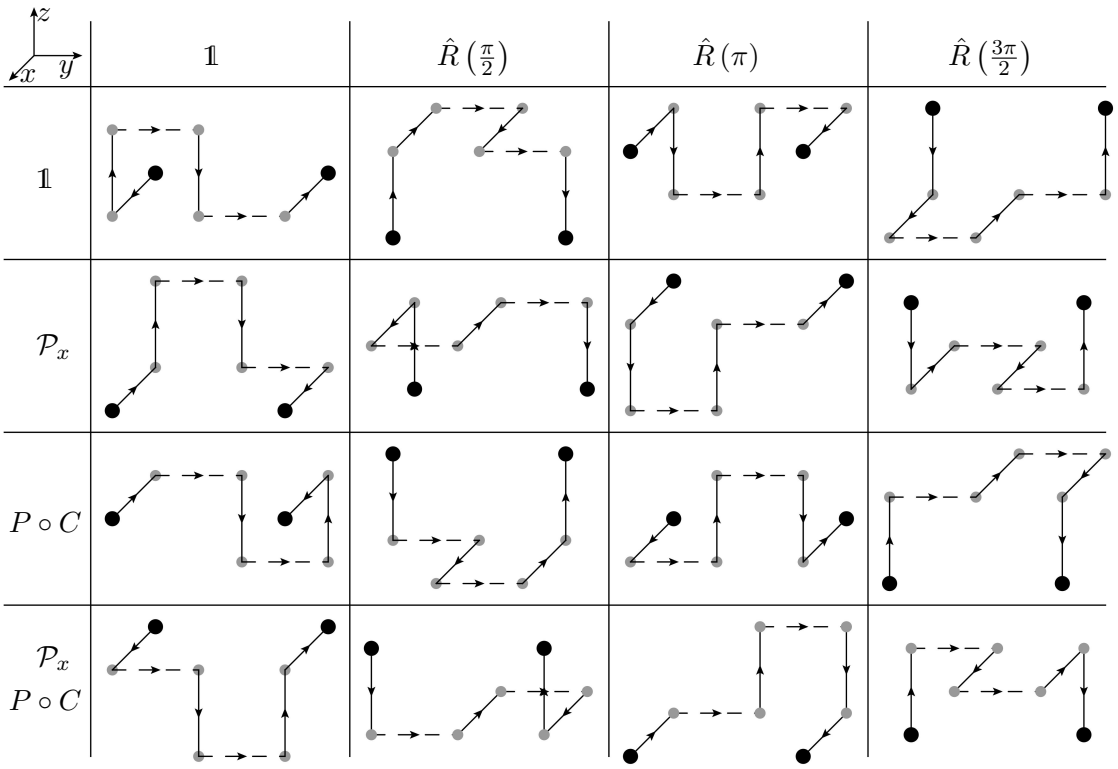

Figure 2.5: An illustration showing all different paths that can appear in $S_{\mathcal{I}}$ defined by (2.58) for the insertion I_6. Each entry in the table is obtained by applying the transformations on the corresponding column and line to the original choice of insertion (upper- and left-most entry in the table).

each Wilson loop over all three possible spatial directions, which are implicitly chosen in (2.62) by choosing a $k \in \{x, y, z\}$ for the quark positions $\mathbf{r}_q, \mathbf{r}_{\bar{q}}$.

Once these Wilson loops are computed, a number of different trial states can be constructed by adding the Wilson loops to obtain the expression (2.62), where the weight factors P_x and Q_{PC} for each loop in the sum are chosen according to (2.58) to obtain the desired quantum numbers. For the maximal case I_6 where each transformation yields a different path on the lattice, all combinations of quantum numbers are possible. For other types of insertions, some transformations may result in the same path on the lattice, which limits our choice of quantum numbers for these types of insertions (cf. Tab. 2.1). For example, applying $\mathcal{P} \circ \mathcal{C}$ to the insertion I_2 does not change the path at all, i.e. $\mathcal{P} \circ \mathcal{C}\, I_2 = I_2$. Inserting this relation into $S_{\mathcal{I}}$, we see that

$$S_{\mathcal{I}(I_2)} \propto (1 + Q_{PC})(1 + P_x \mathcal{P}_x) S_{|L|}(I_2), \tag{2.63}$$

which is zero for $Q_{PC} = -1$, so I_2 cannot be used to construct a trial state with this quantum number.

2.3.2 Analyzing data and determining operator content

Finally, we want to obtain the effective potential (2.4) from the data and fit a constant to the plateau at large time separations to obtain the static quark potentials. To achieve this, we implemented a modern version of the generalized eigenvalue problem (GEVP), as described in [5]. As we have a set of multiple insertions I_j available to construct each trial state (cf. Tab. 2.1), we not only want to compare the quality of each insertion for each possible hybrid static potential, but also find an optimal linear combination of insertions which can be used to construct a state with the largest possible overlap with the desired hybrid state. This guarantees that we obtain an effective potential which reaches a plateau at the smallest possible time separation for our choice of operators. This is important to be able to fit the potential $V(R)$ for each R with small statistical errors, because the signal to noise ratio is still large at small time separations.

In order to find such an optimal linear combination, we have to solve the GEVP not just for the correlation function (2.62) where the insertion is the same at both timeslices t_0 and t_1, but for a correlation matrix, with elements

$$\begin{aligned} C_{jk} = \mathrm{Tr}\big[& U^{t_0}(-R, -d)\, S^{t_0}_{\mathcal{I}(I_j)}(-d, d)\, U^{t_0}(d, R)\, T(t_0, t_1, \mathbf{r}_q) \\ & \Big\{ U^{t_1}(-R, -d)\, S^{t_1}_{\mathcal{I}(I_k)}(-d, d)\, U^{t_1}(d, R) \Big\}^\dagger T^\dagger(t_0, t_1, \mathbf{r}_{\bar{q}}) \big], \end{aligned} \tag{2.64}$$

with different insertions at both timeslices. Here, I_j, I_k are all insertions that can be used to construct the desired trial state given by a fixed choice of $|L|, P_x, Q_{PC}$ in $S^{t_0}_{\mathcal{I}(I_j)}$ and $S^{t_1}_{\mathcal{I}(I_k)}$. We then have to compute a total number of $(12 \times 4)^2 = 2304$ Wilson loop averages for each spatial- and temporal- extension on each lattice configuration to obtain an optimal linear combination of operators for all possible hybrid static potentials (where 12 is the total number of different paths we can construct for our choice of insertions by applying $\mathcal{P}_x$ and $\mathcal{P} \circ \mathcal{C}$ transformations as described in the previous section).

Once a correlation matrix for a trial state is set up, we can solve the GEVP defined by

$$C(t)\,\mathbf{v}_n(t,\tau) = \lambda_n(t,\tau)\,C(\tau)\,\mathbf{v}_n(t,\tau), \tag{2.65}$$

where $\lambda_n(t,\tau)$ are the eigenvalues associated to the eigenvectors $\mathbf{v}_n(t,\tau)$ of the correlation matrix C. We multiply (2.65) from the left with the inverse correlation matrix

$$C^{-1}(\tau)\,C(t)\,\mathbf{v}_n(t,\tau) = \lambda_n(t,\tau)\,\mathbf{v}_n(t,\tau), \qquad t > \tau \tag{2.66}$$

and solve the resulting eigenvalue problem for the matrix $C^{-1}(\tau)\,C(t)$ to obtain the eigenvalues $\lambda_n(t,\tau)$ and eigenvectors $\mathbf{v}_n(t,\tau)$. The same procedure is repeated to obtain $\lambda_n(t+a,\tau)$ and $\mathbf{v}_n(t+a,\tau)$. Finally, we can calculate the value of the effective potential in units of the lattice spacing using the relation (cf. [5])

$$a\,V_{\mathrm{eff},n}(t) = -\ln\left(\frac{\lambda_n(t+a,\tau)}{\lambda_n(t,\tau)}\right), \tag{2.67}$$

where n labels the energy levels, $n=0$ being the ground state. The eigenvalues λ_n are sorted from largest to smallest $\lambda_n \geq \lambda_{n+1}$, so that λ_0 is the largest eigenvalue. The parameter τ, we set to $\tau = 0$. In this way, we obtain the effective potential for the linear combination of chosen operators, which is optimized to have the largest overlap to the hybrid state at the n-th energy level. Errors are computed using a jackknife algorithm.

To gain further insight into our operator choice and identify the contribution of each of our operators to the given hybrid state, we can investigate the eigenvectors $\mathbf{v}_n$, which are also sorted from largest to smallest associated eigenvalue. One can show that the vectors

$$\mathbf{u}_n(t) = \frac{C(\tau)\,\mathbf{v}_n(t)}{|C(\tau)\,\mathbf{v}_n(t)|} \tag{2.68}$$

provide information on the contribution of the operators to the hybrid state (cf. [13]). Specifically, the absolute value of the of j-th component of the vector $\mathbf{u}$

$$\left|\mathbf{u}_n^{(j)}\right|^2 \tag{2.69}$$

is a measure of which fraction of the overlap of a trial state, constructed with the optimal linear combination of operators, with the hybrid state of the n-th energy level is due to the j-th operator.

Lastly, we mention that all operators are constructed using real valued weights, since complex weight factors were not necessary in any of our considerations so far. Since the correlators are lattice path integrals with the plaquette action (2.12), which is invariant under charge conjugation, the correlators are also invariant under charge conjugation, i.e. $C_{jk} = C_{jk,\mathcal{C}}$. Also, because of (2.36), it is $U_{\mathcal{C}} = (U^\dagger)^T = U^*$. Since all our operators are linear combinations of products of links with real valued weights, also the correlators of these operators must fulfill $C_{jk,\mathcal{C}} = C_{jk}^*$ and thus the correlators are real valued,

$C_{jk} = C_{jk,C} = C^*_{jk}$. To verify this relation, we computed the imaginary part of the correlators as an average of the imaginary parts of the corresponding Wilson loops over all lattice configurations and found that indeed, the imaginary part vanishes withing statistical errors. This observation was used to simplify our implementation of the GEVP.

2.4 Decays of hybrid mesons

Hybrid mesons are states with excitations that are caused by gluons. As such, there are possibilities for them to decay into lighter states. Here we will give a short consideration of possible decay channels.

The first quantum number we have to consider is Isospin I. In the case of static potentials with localized heavy quarks, light quarks are not present, so we have Isospin $I = 0$ for all hybrid states considered in this work. To conserve Isospin, it follows that decays into particles with Isospin $I \neq 0$ must include at least two such particles, to make a combination to $I = 0$ possible.

The angular momentum quantum number L of our hybrid meson states is defined by the rotational symmetry around the separation axis of the quark antiquark pair. To conserve this quantum number in a decay process, we require that the relative angular momentum of the decay products with respect to this distinguished axis, which we call $\ell_{z,\text{out}}$, is conserved. This means that the total relative angular momentum ℓ_{out} of decay products can have additional components with respect to an axis that is perpendicular to this axis. Additionally, the contribution to parity of relative angular momentum, which is a factor $(-1)^{\ell_{\text{out}}}$, has to be taken into account. However, this additional contribution to parity can be chosen freely, because an upper limit to the relative angular momentum ℓ_{out} is not given. The conservation of the quantum number of the hybrid mesons defined by the combination of parity and charge conjugation can then also be conserved in the decay process by choosing a suitable ℓ_{out}.

One possible decay is for example

$$\Pi_u \longrightarrow \Sigma_g^{\pm} + n\,\pi.$$

For this decay, the number of outgoing pions must be $n \geq 2$ to conserve Isospin. To conserve $L = 1$ with pions which have angular momentum $L_\pi = 0$, the relative angular momentum of the decay products must be $\ell_{\text{out}} \geq 1$. For $n = 2$, the total combined $\mathcal{P}$- and $\mathcal{C}$-parity of the decay products is $(+)$. Choosing $\ell_{\text{out}} = 1$ contributes an additional minus sign, so that $\mathcal{PC}$-parity is conserved, as the hybrid state Π_u has $Q_{PC} = -$. Similarly, for $n = 3$, we choose an outgoing relative angular momentum so that $\ell_{z,\text{out}} = 1$ and $\ell_{\text{out}} = 2$, which compensates the sign change in total parity coming from the additional pion. The possible number of outgoing pions is then only restricted by the mass difference of the in- and outgoing heavy (hybrid) mesons.

3 Results

In this section we show the hybrid static potentials from our numerical computations, including all insertions shown in figure 2.4a. Static potentials have been computed for all possible states that can be created using these operators, as listed in table 2.1. We show the lattice setup and some prior optimization of the generation of gauge configurations, smearing, and operator choice. Additionally, we look at some excited energy levels and the overlaps the states created by each of our operators have with the hybrid states.

3.1 Lattice setup

We generated lattice configurations in pure SU(3) gauge theory using the Wilson plaquette action (2.12). For this, we used the heatbath algorithm of the Chroma Library for Lattice Field Theory [1]. We have generated 700 gauge configurations with a lattice size of $24^3 \times 48$ with $\beta = 6.0$, which corresponds to a lattice spacing of $a \approx 0.093\,\text{fm}$. The lattice spacing was computed with the sommer parameter, using the method described in section 2.1.3. A sufficiently small autocorrelation between the generated configurations has been verified using binning with multiple binning sizes (Fig. 3.1).

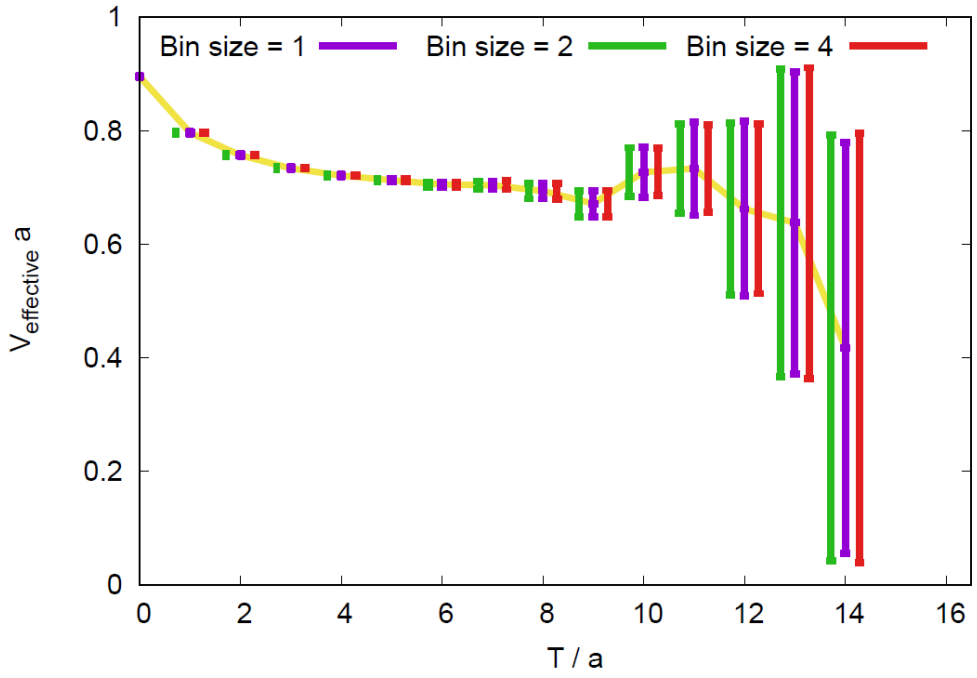

Figure 3.1: Binning of 700 configurations for the ordinary static potential at spatial quark pair separation $R = 12a$ with binning sizes $1, 2, 4$. Error bars for binning sizes $2, 4$ have been shifted for better visibility.

3.2 APE smearing

Effective potentials have been computed at $T = 1$ for different numbers of APE smearing steps n_{APE} to find an optimal choice, i.e. one where the plateau is reached fastest (Fig.3.2). The lowest effective mass for the Δ_g^+ potential is at $n_{\text{APE}} = 10$. For the Π_u potential, V_{eff} is a bit lower at $n_{\text{APE}} = 20$, but still reasonable for $n_{\text{APE}} = 10$. As the higher angular momentum potential has larger errors for computations over an equal number of configurations, we chose $n_{\text{APE}} = 10$ to compute the hybrid potentials in this section. For the ordinary potential 3.2 (a) at $n_{\text{APE}} = 100$, the effective potential seems to reach a maximum, which is an unusual dependence on n_{APE}, however, these computations were done on a smaller set of 50 configurations, and errors are not available. It is possible this maximum only occurs within statistical error.

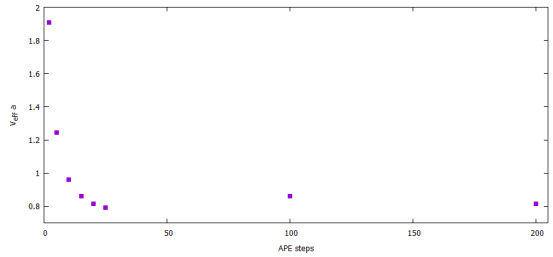

(a) Ordinary static potential Σ_g^+ computed with regular planar Wilson loops.

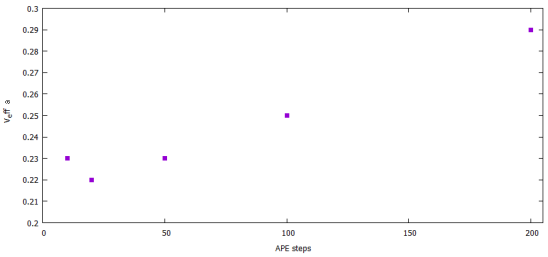

(b) Ordinary potential Σ_g^+, computed with the short staple operator I_0.

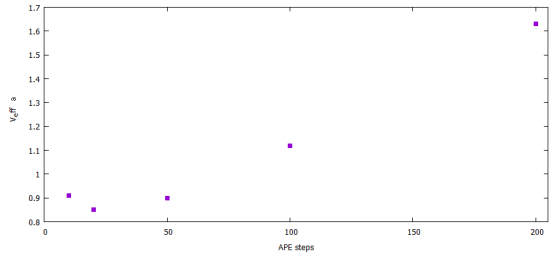

(c) Π_u potential

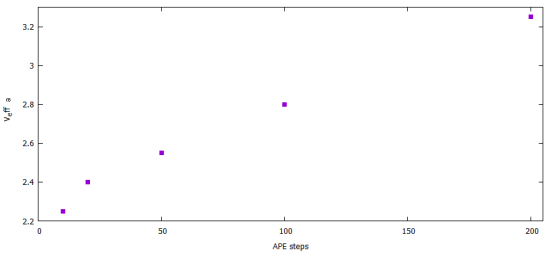

(d) Δ_g^+ potential

Figure 3.2: Effective masses of hybrid potentials at T = 1 computed with regular planar Wilson loops ((a)), and the short staple operator I_0 ((b) - (d)).

3.3 HYP smearing

We also computed the ordinary static potential with regular Wilson loops with and without HYP smearing for small spatial separations (Fig. 3.3). This computation only includes 100 configurations.

The gap in the effective potential between the quark separations $R = 1$ and $R = 2$ is much smaller when HYP-smearing is used, than it is for the potential without HYP-smearing. The behavior of the potential at $R \lesssim 2$ with HYP smearing is subject to large discretization errors, because the hypercubes over which the links of the Wilson loop in

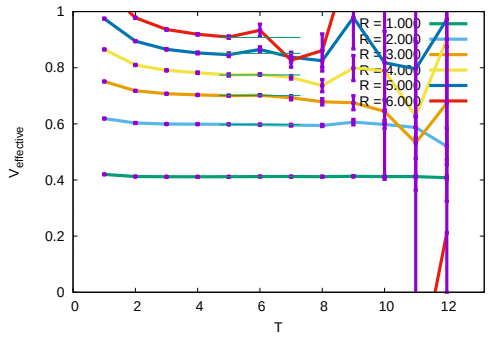

(a) Effective potential without HYP smearing.

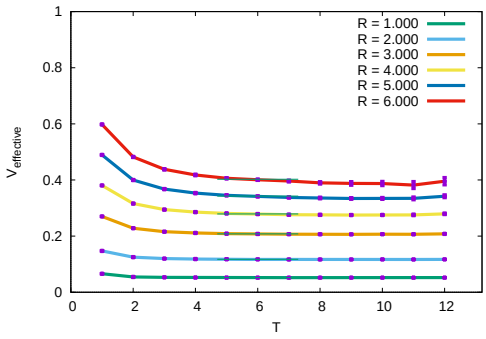

(b) Effective potential with HYP smearing.

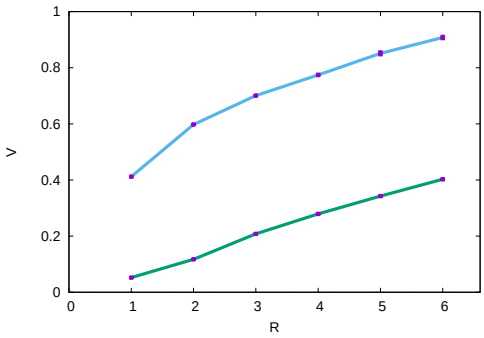

(c) Ordinary static potential without (blue curve) and with (green curve) HYP smearing.

Figure 3.3: Ordinary static potential computed without and with HYP smearing.

time direction are smeared with the HYP algorithm have significant overlap with each other on the lattice at a small spatial separation of just a few lattice sites. Consequently, we have to turn off HYP smearing for small spatial separations, to obtain the correct behavior of the potential. For larger spatial separations however, the hypercubes do not overlap and HYP smearing reduces the errors of the effective potential by a substantial amount, which we can clearly see in figure 3.3.

3.4 Potentials

In this section we show the results for the hybrid potentials we can obtain using our insertions 2.4a. We compute $(12 \times 4)^2$ Wilson loop averages on each of our 700 gauge configurations to include all possible operators and quantum numbers, as outlined in

sections 2.3.1 and 2.3.2. For each configuration, the Wilson loop is averaged over each point on the lattice, and over each direction of its spatial extension. We computed Wilson loop averages in this way for spatial separations $R/a = 2, 3, \ldots, 12$ and temporal separations $T/a = 0, 1, \ldots, 15$. Wilson loops with a spatial separation of $R = 1$ have not been computed, because a part of our operators are not defined for $R < 2$. We note the effective potential is only plotted for temporal separations $T = 0, \ldots, 14$, since we obtain it by solving the GEVP (cf. section 2.3.2), which requires the correlation matrix at two different times as an input for each value of the effective potential.

3.4.1 Ordinary static potential

As a start, the ordinary potential was computed using the simple staple operator I_1 of length R.

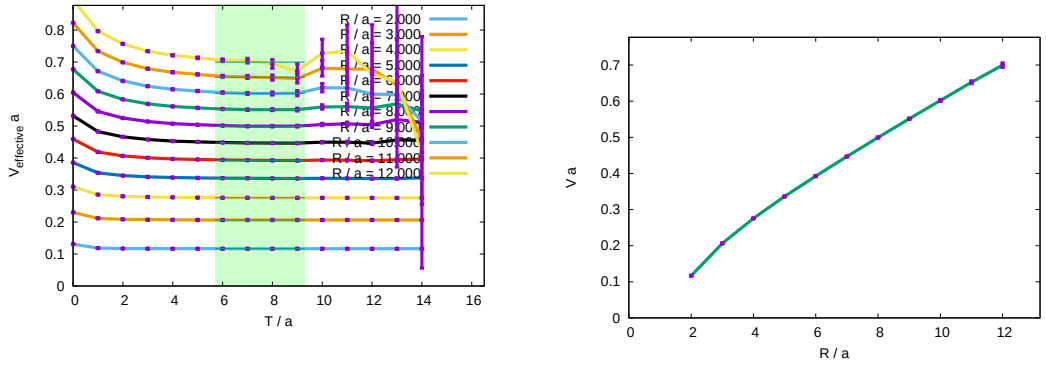

(a) Effective potential. Thin green lines and a green background indicate the range used to fit a constant to the plateau.

(b) Static potential

Figure 3.4: Ordinary potential computed with a simple staple operator of length R.

We obtain the effective potential V_{eff} for each R as a function of the temporal separation T. We then evaluate at which value of T the effective potential reaches a plateau and fit a constant to this range to compute the static potential. This works well for the ordinary static potential (Fig. 3.4).

3.4.2 Short and long insertions

One property of the operators we use to construct the hybrid states, is their extension along the quark antiquark separation axis. This property can easily be transfered to different shapes of insertions, by extending their path of links in direction of the separation axis. To get an idea which type of operator, shorter ones, or more extended ones, are better used to compute hybrid potentials, we compared the effective potentials obtained using the insertions I_0 and I_1, which have a simple and similar shape, that only differs in the extension in direction of the separation axis. Figure 3.5 shows the effective potentials for these insertions for both possible hybrid states (cf. Tab. 2.1).

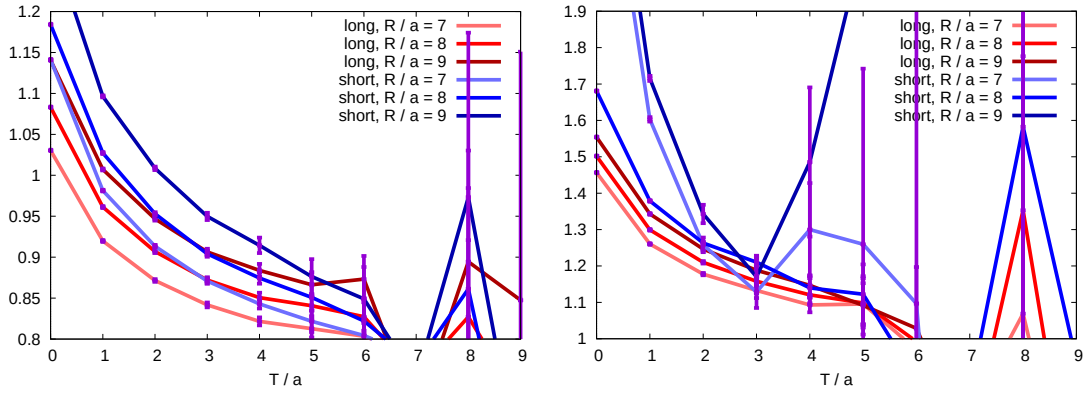

(a) Hybrid state Π_u

(b) Hybrid state Δ_g^+

Figure 3.5: Comparison of effective potentials computed with short staples I_0 (left) and long staples I_1 (right). For these potentials, only 100 configurations were used.

We can clearly see that the effective potentials for the long staples I_1 reach a plateau substantially faster and consequently are better suited to compute the hybrid potentials. Furthermore, the potentials for short stables have a splitting of values for odd and even spatial separations R/a. This effect must originate in the averaging of operators for the case of Wilson loops with even (in the case of short staples, cf. (2.61)) spatial separation. An averaging in this way seems to result in overlaps with different states, as this shift in the effective potential indicates. However, as we will see later, such a splitting does not occur even for more complicated operators that extend over the whole separation axis, while using this same method of averaging for operators that cannot be directly placed on the midpoint of the separation axis. Because of this, the origin of this split for short staples is not clear.

Contributions to the overlaps of the trial states with the hybrid states were also plotted in figure 3.6 for both short and long staples as a function of the quark antiquark separation. Beside statistical errors, none of the overlaps showed any dependence on the temporal separation. The overlaps give further assurance that operators with a bigger

extension along the separation axis are much better suited to compute hybrid potentials. We clearly see that short staples have a small contribution $\left|u_0^{(0)}\right|^2 < 0.2$ to the total overlap with the hybrid state, while the contribution of long staples dominates with $\left|u_1^{(0)}\right|^2 > 0.8$. Furthermore, the contribution of short/long staples decreases/increases as the quark antiquark separation grows larger, indicating that a larger ratio of operator extension to quark separation results in a larger overlap to the hybrid state.

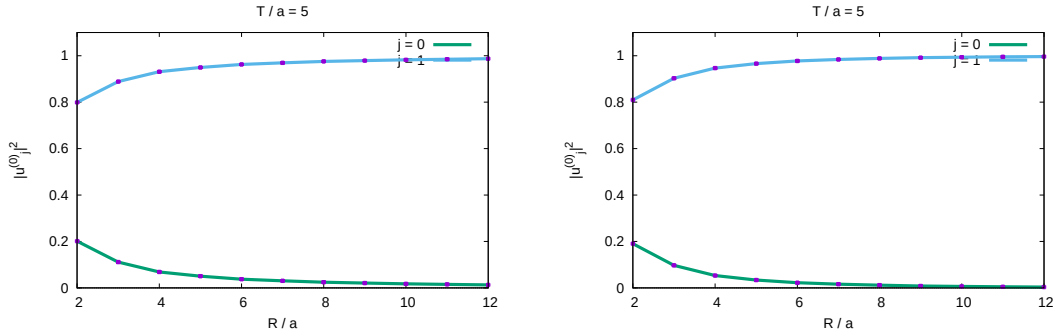

Figure 3.6: Overlaps for short ($j = 0$) and long ($j = 1$) staples with hybrid states Π_u (left) and Δ_g^+ (right)

3.4.3 Hybrid potentials

For the hybrid potentials, we computed Wilson loops for all insertions in Fig. 2.4a. We compute effective potentials for each hybrid state using the correlation matrices which are built using all insertions available to construct the corresponding trial states. Figures 3.7, 3.8, 3.9 show the effective potentials for all these hybrid states. Horizontal, thin green lines and a green background represent the range of temporal separation T/a to which a constant was fitted to obtain the value of the static potential for the greatest possible temporal separation.

For all hybrid states, the error bars of the effective potentials at temporal separations $T \gtrsim 5$ grow much larger than the change in the value of the effective potential for neighboring temporal separations, so a fit of a constant to obtain the static potential should not be done in these regions. Also, a plateau is only reached approximately for some states at smaller spatial separations, in particular the states for angular momentum $L = 1$, namely Π_g, Π_u, and the state Σ_u^- seem to approach a plateau for spatial separation $R/a \lesssim 6$. The state Δ_g^- also seems to approach a plateau for $R/a \lesssim 5$ at $T/a = 4$, however the signal breaks off already after a temporal separation of one additional lattice lattice spacing $T/a = 5$.

Figures 3.10, 3.11, 3.12 show the hybrid states potentials obtained by fitting constants

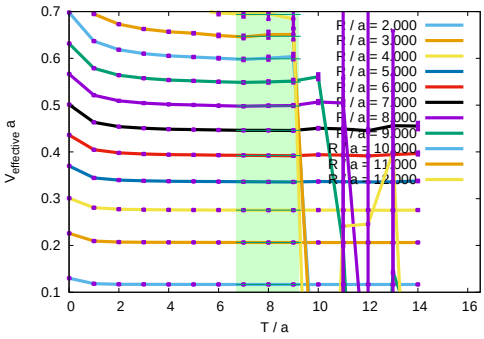

(a) Σ_g^+ (ordinary static potential).

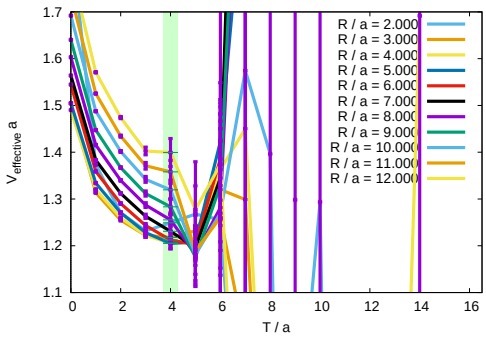

(b) Σ_u^+, includes insertions I_4, I_6.

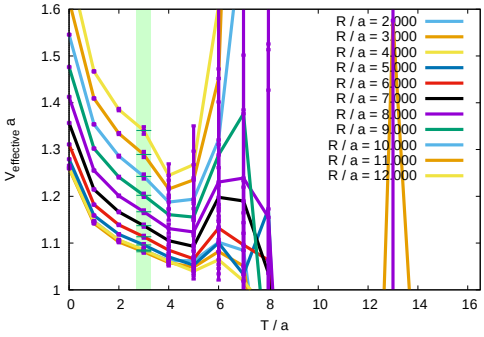

(c) Σ_g^-, includes insertions I_3, I_6.

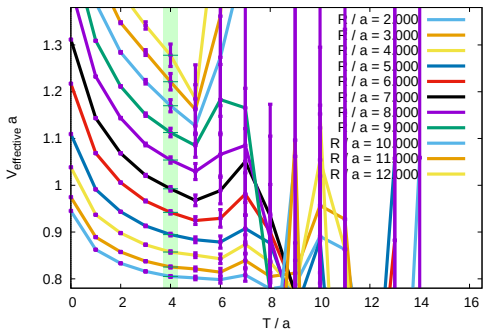

(d) Σ_u^-, includes insertions I_5, I_6.

Figure 3.7: Effective potentials for hybrid states with angular momentum $L = 0$.

to the effective potentials at the indicated values of T/a. All potentials are plotted at the same scale. But we note, that potentials for states other than the mentioned ones should be treated as very crude results, as plateaus are clearly not reached yet for these states.

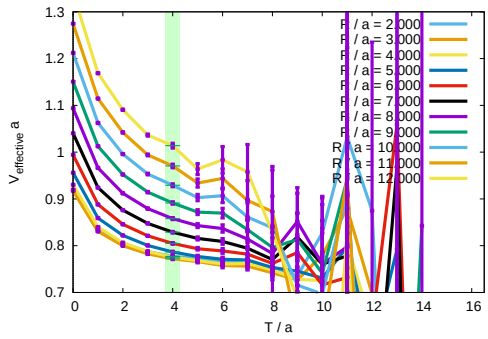

(a) Π_g, includes insertions I_2, I_4, I_5, I_6.

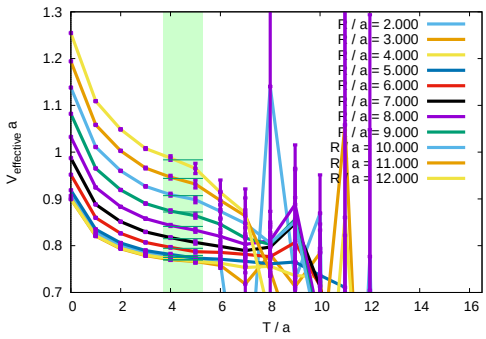

(b) Π_u, includes insertions I_1, I_3, I_4, I_5, I_6.

Figure 3.8: Effective potentials for hybrid states with angular momentum $L = 1$.

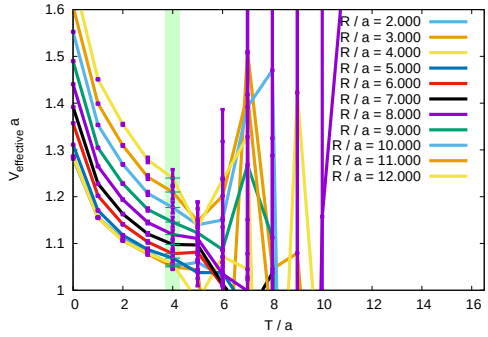

(a) Δ_g^+, includes insertions I_1, I_2, I_3, I_4, I_6.

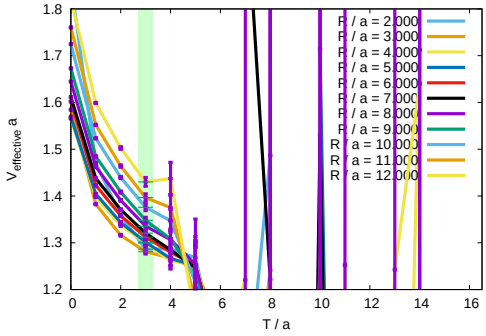

(b) Δ_u^+, includes insertions I_4, I_5, I_6.

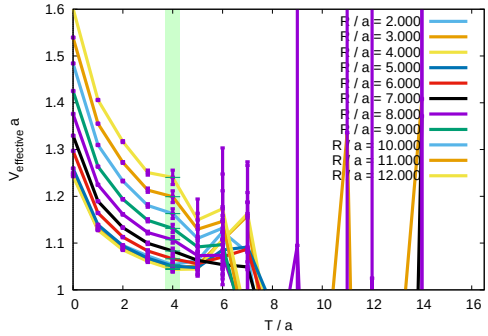

(c) Δ_g^-, includes insertions I_3, I_5, I_6.

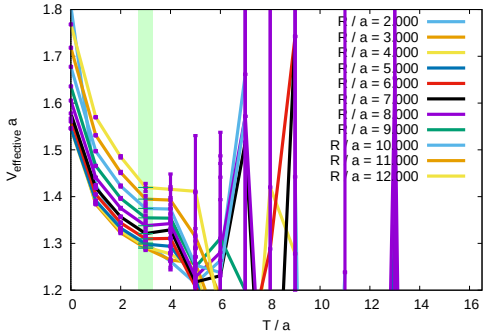

(d) Δ_u^-, includes only insertions I_6.

Figure 3.9: Effective potentials for hybrid states with angular momentum $L = 2$.

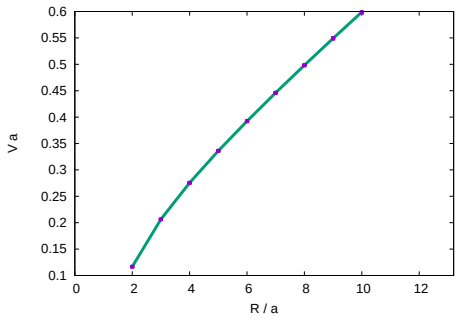

(a) Σ_g^+ (ordinary static potential).

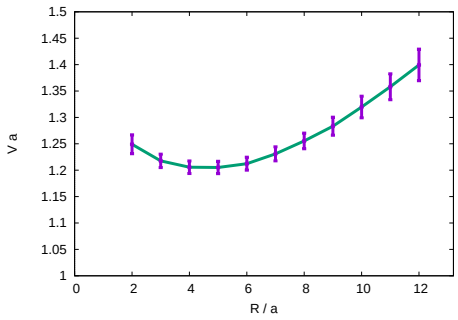

(b) Σ_u^+, includes insertions I_4, I_6.

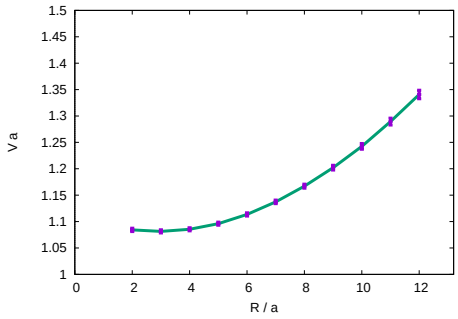

(c) Σ_g^-, includes insertions I_3, I_6.

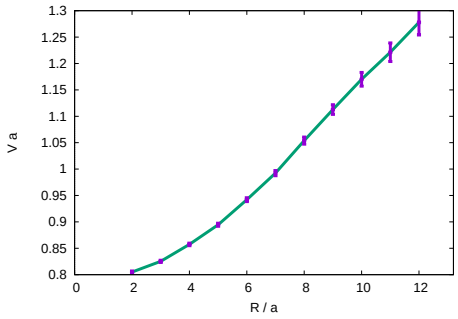

(d) Σ_u^-, includes insertions I_5, I_6.

Figure 3.10: Effective potentials for hybrid states with angular momentum $L = 0$.

Almost all potentials seem to exhibit a repulsive behavior at very small separations, but again we stress that most potentials are very crude results and in particular the Σ_u^- potential, which is the state for which the effective potential reached a plateau for small spatial separations, does not show a repulsive behavior. However, a positive curvature at very small spatial separations is still visible. These are first results, and one should investigate the potentials also at smaller lattice spacing and smaller spatial separations and to gain more insight into this potentially repulsive property of the hybrid potentials.

Also, we observe that the quantum number P_x seems to have a small influence on the properties of hybrid potentials with angular momentum $L = 2$, as the potentials and effective potentials of the states Δ_g^+ and Δ_g^-, as well as Δ_u^+ and Δ_u^- are very similar. This is expected, since hybrid states with $|L| > 0$ have no preferred orientation of their angular momentum so the states with $L = 2$ and $L = -2$ are degenerate. The reflection corresponding to the P_x quantum number flips the orientation of the angular momentum and transforms these states into each other, consequently states with different P_x are degenerate (cf. [4]).

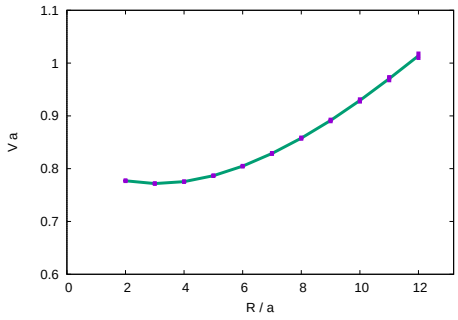

(a) Π_g, includes insertions I_2, I_4, I_5, I_6.

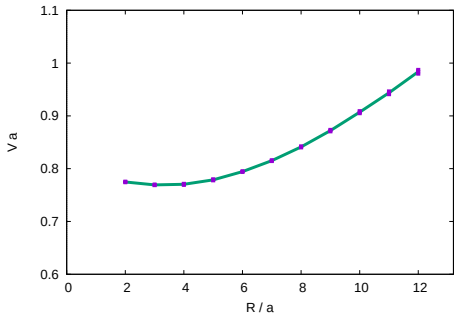

(b) Π_u, includes insertions I_1, I_3, I_4, I_5, I_6.

Figure 3.11: Effective potentials for hybrid states with angular momentum $L = 1$.

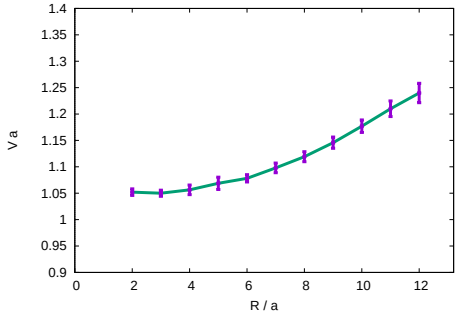

(a) Δ_g^+, includes insertions I_1, I_2, I_3, I_4, I_6.

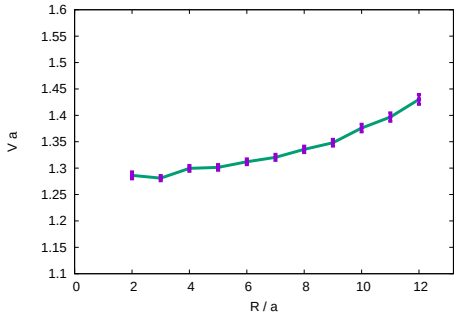

(b) Δ_u^+, includes insertions I_4, I_5, I_6.

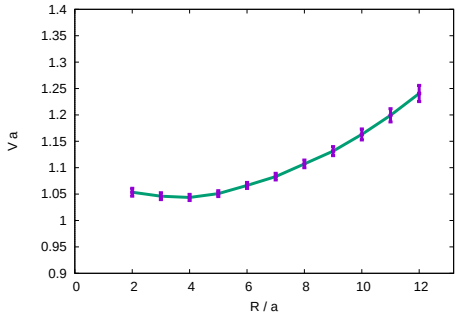

(c) Δ_g^-, includes insertions I_3, I_5, I_6.

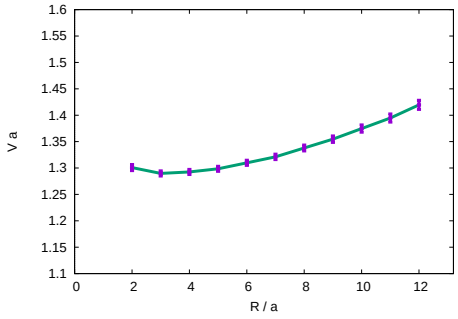

(d) Δ_u^-, includes only insertions I_6.

Figure 3.12: Effective potentials for hybrid states with angular momentum $L = 2$.

3.4.4 Operator overlaps

To compute the static potentials via a fit of a constant to the plateau of the effective potential at large times, it is important that the generated trial states have large overlaps to the extracted energy eigenstates. To gain some insight into which of our insertions shown in Fig. 2.4a are best suited to generate trial states with large overlaps to the energy eigenstates, we show each operators contribution to the total overlap of the trial state with the extracted energy eigenstate in figures 3.13, 3.14, 3.15. Here, $\left|u_j^{(0)}\right|^2$ is the contribution of the operator, which is constructed with the insertion I_j, to the total overlap of the trial state to the ground state. Operator overlaps for the state Δ_u^- are omitted, since only a single operator was used to construct the associated trial state.

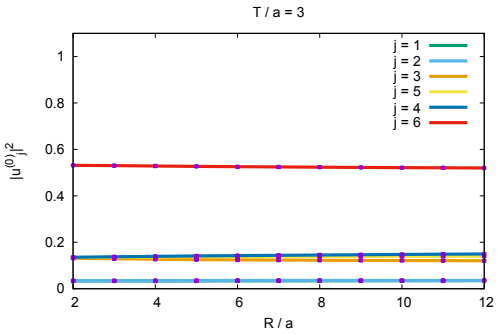

(a) Σ_g^+ (ordinary static potential).

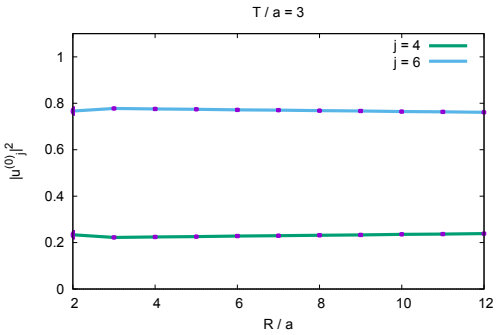

(b) Σ_u^+, includes insertions I_4, I_6.

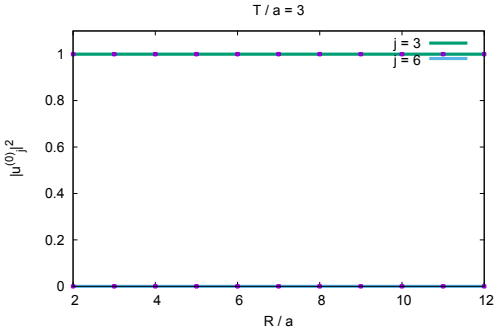

(c) Σ_g^-, includes insertions I_3, I_6.

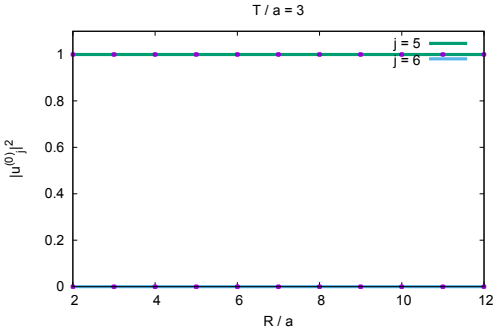

(d) Σ_u^-, includes insertions I_5, I_6.

Figure 3.13: Operator overlaps for hybrid states with angular momentum $L = 0$.

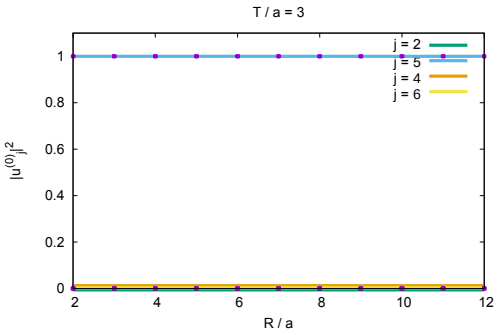

(a) Π_g, includes insertions I_2, I_4, I_5, I_6.

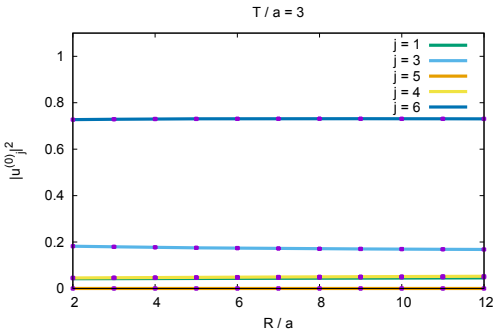

(b) Π_u, includes insertions I_1, I_3, I_4, I_5, I_6.

Figure 3.14: Effective potentials for hybrid states with angular momentum $L = 1$.

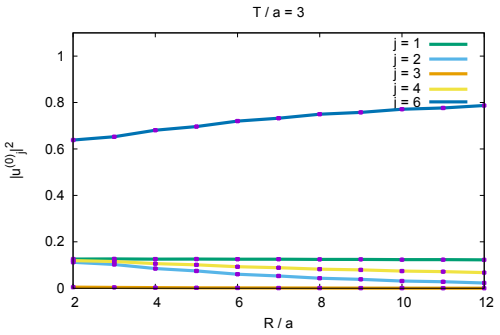

(a) Δ_g^+, includes insertions I_1, I_2, I_3, I_4, I_6.

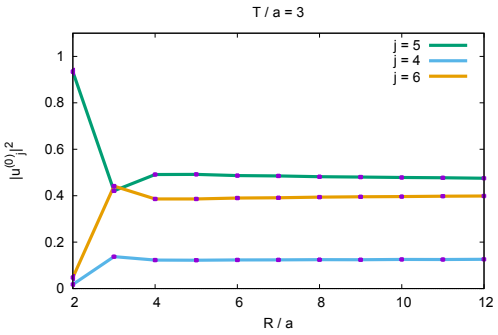

(b) Δ_u^+, includes insertions I_4, I_5, I_6.

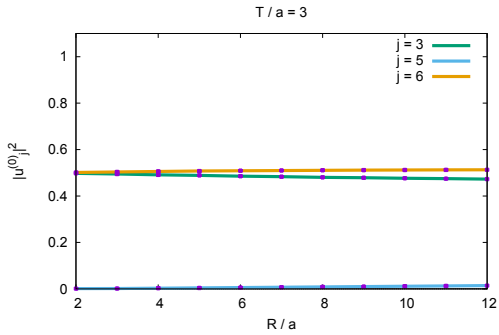

(c) Δ_g^-, includes insertions I_3, I_5, I_6.

Figure 3.15: Effective potentials for hybrid states with angular momentum $L = 2$.

We observe that the more complicated operators I_5 and I_6 significantly dominate the overlaps of all hybrid states, except for the state Σ_g^-. However, only the insertions I_3, I_6 were available to construct this particular state, while I_6 shows a vanishing contribution to hybrid states of angular momentum $L = 0$ with quantum number $P_x = -$. Following the trend, we expect more complicated shapes that we did not include, to have significantly larger contributions to the overlap also for this state. In contrast, simple shapes like insertions I_1, I_2, I_3, I_4 have much smaller contributions to the overlap than more complicated ones, for all considered hybrid states.

3.4.5 Orthogonal states, excited states

Finally, to ascertain the correctness of our algorithms, simulation- and analysis- codes, a cross-check was done and compared to expected results. As discussed in section 2.2.3, in theory one can assign the quantum number P_x also to the hybrid states of angular momentum $L = 1$, namely Π_g and Π_u to obtain two orthogonal states. In the results shown so far, these states were generated with the choice $P_x = -$ for our particular choice of coordinate system.

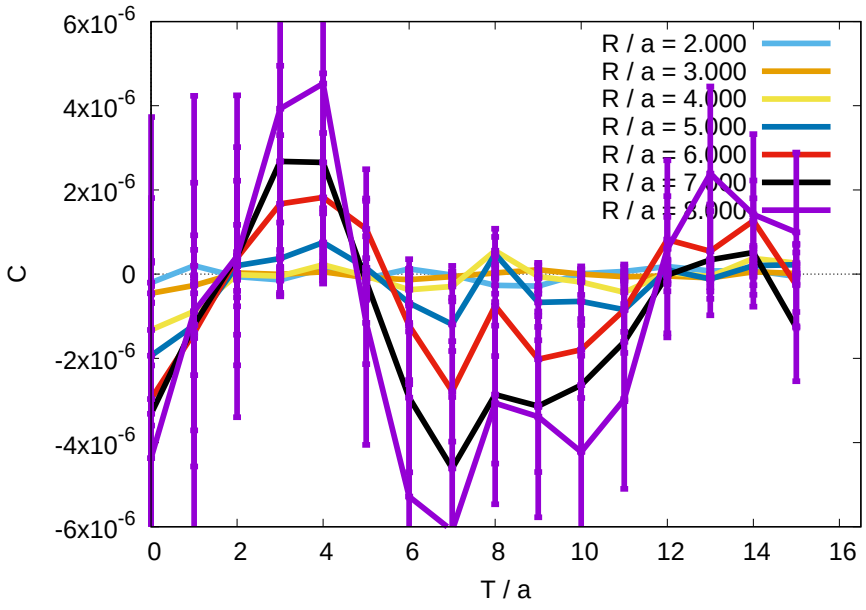

Figure 3.16: Correlator $C = \langle\Omega|\ \mathcal{O}^\dagger_{\Pi_g^+}(T)\,\mathcal{O}_{\Pi_g^-}(0)\ |\Omega\rangle$ of the operators for the two orthogonal states Π_g^+, Π_g^-.

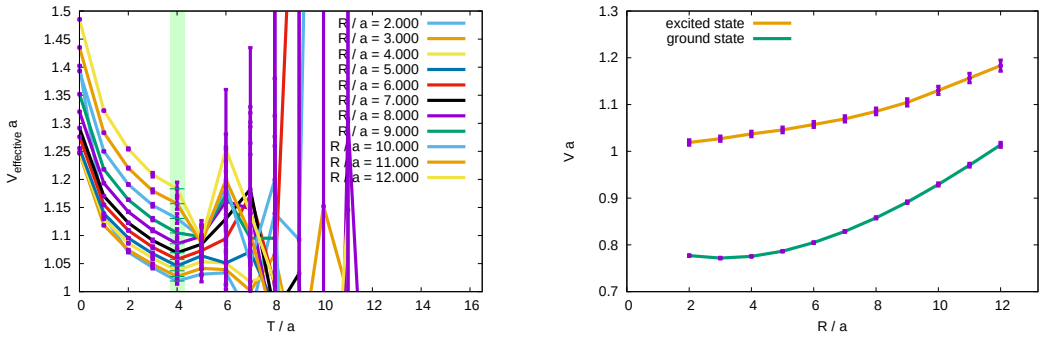

(a) Excited Π_g state.

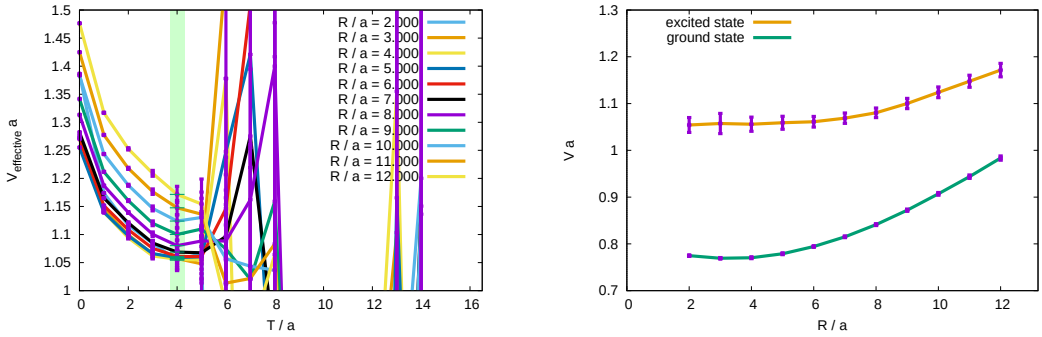

(b) Excited Π_u state.

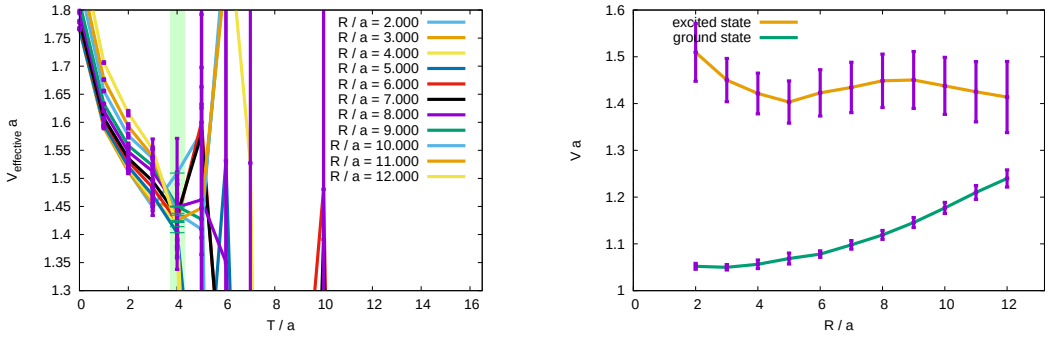

(c) Excited Δ_g^+ state.

Figure 3.17: Effective potentials for first excited hybrid states.

Now, we also generated an orthogonal trial state with $P_x = +$ and computed the correlator of the two operators which create the two orthogonal states 'Π_g^+, Π_g^-'. A plot of the correlator is shown in Fig. 3.16, and it is indeed zero within statistical errors.

Furthermore, excited potentials were computed for the states Π_g, Π_u, Δ_g^+, and are shown in Fig. 3.17. While none of the effective potentials reach a clear plateau, they have the expected shape. The shapes of the excited state potentials are just a very crude estimate, since no plateau is reached, but it is clear that they lie significantly above the ground state potentials, as one would expect.

4 Conclusion

4.1 Summary

The goal of this work was to get a better understanding of hybrid static potentials and of methods to compute these using lattice simulations. We examined these hybrid static potentials in SU(3) Yang-Mills theory to realize the excitations of these quark antiquark states in the gluon sector, which ultimately meant the computation of Wilson loops with specific insertions. We obtained a rigorous understanding of how to construct trial states within the given theory from different kinds of operators and which effect the choice of these operators have on the quantum numbers of the resulting trial states. Furthermore, we obtained hybrid static potentials for the states $\Sigma_g^+, \Sigma_g^-, \Sigma_u^+, \Sigma_u^-, \Pi_g, \Pi_u, \Delta_g^+, \Delta_g^-, \Delta_u^+, \Delta_u^-$ which covers all possible combinations of quantum numbers up to angular momentum $L = 2$ and investigated different kinds of operators for each state. We concluded that more extended, non-local operators, as well as operators with more intricate structures on the lattice are much better suited for all states, than local operators and operators with simple shapes are. In addition, correlators of orthogonal states and hybrid static potentials of some excited states were computed and showed the expected behavior, which is a strong verification of the correctness of the methods used in this work. The final potentials were computed for a lattice spacing of $a \approx 0.093\,\text{fm}$ on 700 gauge configurations and are shown in Fig. 4.1 alongside results for the same states from an earlier work [10]. While the results of [10] are given for a larger range of quark antiquark separations and seem to have smaller statistical errors, plots of effective potentials, or a clear procedure of how these potentials were obtained, are not shown. Our results are largely in agreement with those of [10], and we also show effective potentials to give a clear demonstration of which aspects still need to be improved on. Only our results for the Π_g state seem to disagree with [10], however the overlaps in Fig. 3.14 show that only one operator contributed to this particular state, so this could mean that this operator does also not have a sufficient overlap with the hybrid state.

Furthermore, the construction and analysis of suitable trial states was shown in detail, and tools were created to compute hybrid static potentials with any arbitrary choice of operators, so more shapes can easily be investigated. The tools were set up in a way, which allows the computation of more complicated operators at a relatively low cost of

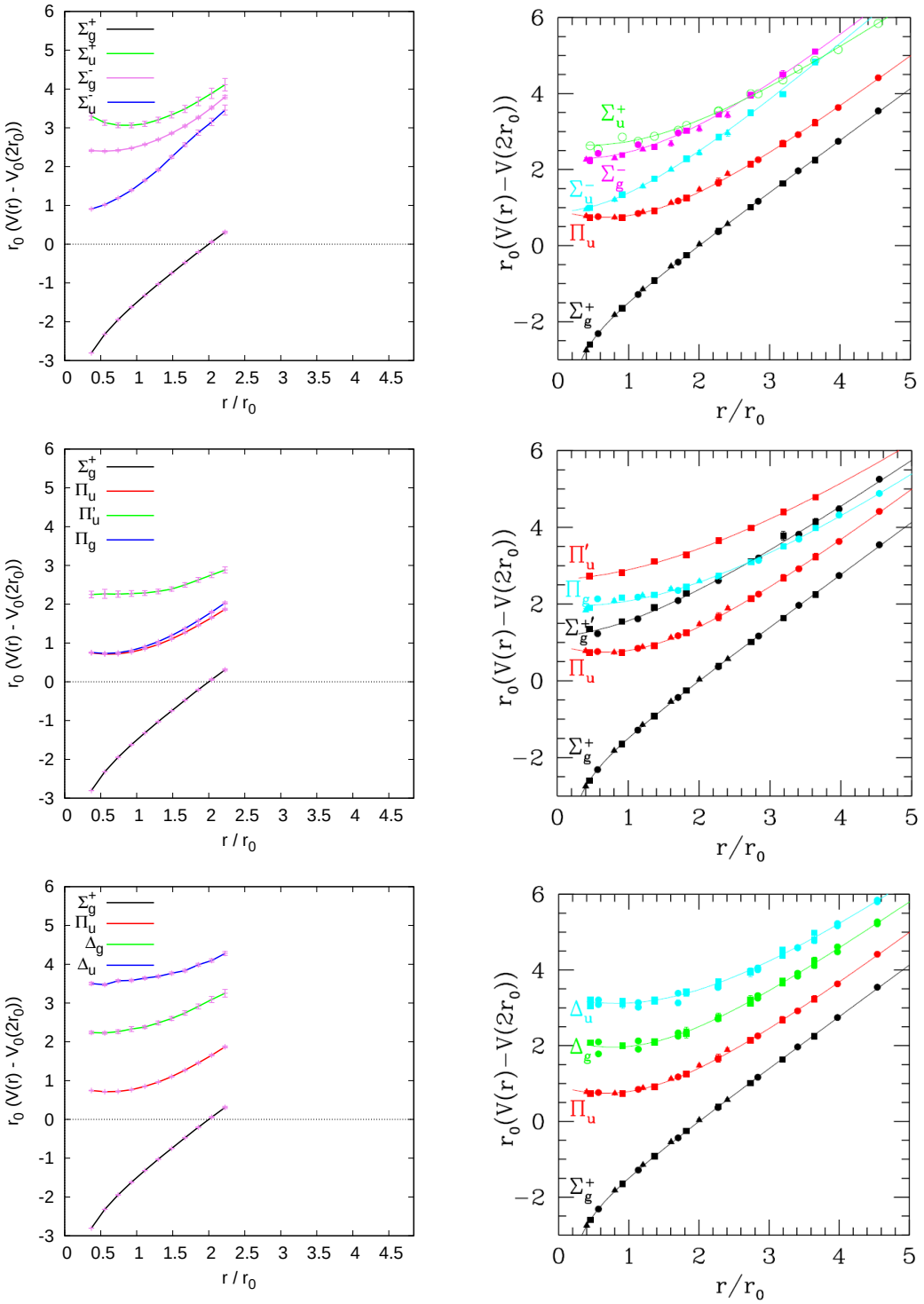

Figure 4.1: Our results (left) for the static potentials of various hybrid states compared to the results of the work [10] (right).

computation time compared to the computation time needed to compute the final correlators, as long as the symmetry properties of the operator, corresponding to angular momentum, $\mathcal{P} \circ \mathcal{C}$-parity, and the quantum number P_x, stay unchanged.

4.2 Outlook

To contribute to a deeper understanding of the strong interaction, research of exotic matter such as the hybrid states discussed in this work, is essential. With the established methods, an obvious next step is to consider operators which are expected to be able to construct trial states with larger overlaps with the states of interest and to also compute the hybrid static potentials on a larger number of lattice gauge configurations to directly decrease statistical errors, as well as to compute these on lattices with different lattice spacings to obtain potentials for a wider range of quark antiquark separations and investigate discretization effects.

A next step will be to match the results of these lattice computations to perturbative results and develop methods to compute the hybrid potentials in full dynamical QCD. Potentials obtained in this way can then be used to solve Schrödinger equations and make predictions for the masses of such states. Such results are of interest with regard to the PANDA experiment at FAIR, which is planned to also search for hybrid meson states. In particular, a detailed understanding of masses and possible sufficiently stable states will allow for a systematic analysis of the experimental data. Furthermore, effects of quark spins on these states are known to be significant, and methods to include such effects also need to be investigated to gain a full understanding of hybrid states.

References

[1] The chroma library for lattice field theory. http://jeffersonlab.github.io/chroma/. Date: June 2016.

[2] Panda experiment website. https://panda.gsi.de/oldwww/. Date: 2017.

[3] Gunnar S. Bali, Bram Bolder, Norbert Eicker, Thomas Lippert, Boris Orth, Peer Ueberholz, Klaus Schilling, and Thorsten Struckmann. Static potentials and glueball masses from QCD simulations with Wilson sea quarks. *Phys. Rev.*, D62:054503, 2000, hep-lat/0003012.

[4] Matthias Berwein, Nora Brambilla, Jaume Tarrus Castella, and Antonio Vairo. Quarkonium hybrids with nonrelativistic effective field theories. 2015, arXiv:1510.04299.

[5] B. Bloisser, M.D. Morte, G.v. Hippel, T. Mendes, and R. Sommer. On the generalized eigenvalue method for energies and matrix elements in lattice field theory. arXiv:0902.1265v2 [hep-lat], 2009.

[6] N. A. Campbell, A. Huntley, and Christopher Michael. Heavy Quark Potentials and Hybrid Mesons From SU(3) Lattice Gauge Theory. *Nucl. Phys.*, B306:51–62, 1988.

[7] C. Gattringer and C.B. Lang. *Quantum Chromodynamics on the Lattice*. Springer, 2010.

[8] A. Huntley and Christopher Michael. Static Potentials and Scaling in SU(2) Lattice Gauge Theory. *Nucl. Phys.*, B270:123–134, 1986.

[9] K. Jansen, C. Michael, A. Shindler, and M. Wagner. The static-light meson spectrum from twisted mass lattice qcd. arXiv:0810.1843v1 [hep-lat], 2008.

[10] K. J. Juge, J. Kuti, and C. J. Morningstar. Gluon excitations of the static quark potential and the hybrid quarkonium spectrum. *Nucl. Phys. Proc. Suppl.*, 63:326–331, 1998, hep-lat/9709131.

[11] K. Jimmy Juge, Julius Kuti, and Colin Morningstar. Fine structure of the QCD string spectrum. *Phys. Rev. Lett.*, 90:161601, 2003, hep-lat/0207004.

[12] K. Jimmy Juge, Julius Kuti, and Colin Morningstar. The heavy-quark hybrid meson spectrum in lattice qcd. 2003, arXiv:nucl-th/0307116.

[13] M. Kalinowski and M. Wagner. Masses of d mesons, d_s mesons and charmonium states from twisted mass lattice qcd. arXiv:1509.02396v1 [hep-lat], 2015.

[14] C. A. Meyer and E. S. Swanson. Hybrid mesons. 2015, arXiv:1502.07276.

[15] C. Michael. Hybrid mesons from the lattice, 2003, arXiv:hep-ph/0308293.

[16] Chris Michael. Hadronic spectroscopy from the lattice: Glueballs and hybrid mesons. 1998, arXiv:hep-ph/9810415.

[17] Chris Michael. Quarkonia and hybrids from the lattice, 1999, arXiv:hep-ph/9911219.

[18] C. Morningstar, K. J. Juge, and J. Kuti. Gluon excitations of the static quark potential. In *Quark confinement and the hadron spectrum III. Proceedings, 3rd International Conference, Newport News, USA, June 7-12, 1998*, pages 179–182, 1998, hep-lat/9809015.

[19] Mike Peardon. Coarse lattice results for glueballs and hybrids. 1997, arXiv:hep-lat/9710029.

[20] S. Perantonis, A. Huntley, and Christopher Michael. Static Potentials From Pure SU(2) Lattice Gauge Theory. *Nucl. Phys.*, B326:544–556, 1989.

[21] S. Perantonis and Christopher Michael. Static potentials and hybrid mesons from pure SU(3) lattice gauge theory. *Nucl. Phys.*, B347:854–868, 1990.

[22] H.J. Rothe. *Lattice gauge theories.* World Scientific, 2015.

[23] D. Toussaint. Glueballs and hybrids (gluons as constituents). 1999, arXiv:hep-lat/9909088.

[24] M. Wagner. An introduction to lattice hadron spectroscopy for students without quantum field theoretical background. arXiv:1310.1760v1 [hep-lat], 2013.

[25] P. Wolf. Hybrid static potentials in su(2) yang-mills theory on the lattice, 2012.

Acknowledgments

I want to thank Marc Wagner in particular for a great supervision and the frequent helpful discussions on the topic. I also want to thank Stefano Capitani for joining the discussions and helping to verify the correctness of the tools we used by creating an independent second version, as well as Joshua Berlin for assisting with the setup and usage of the Chroma Library and computer clusters.